



HAL
open science

CFD modeling of mass transfer in Gas-Liquid-Solid catalytic reactors

Hanane Bouras, Yacine Haroun, Régis Philippe, Frédéric Augier, Pascal Fongarland

► **To cite this version:**

Hanane Bouras, Yacine Haroun, Régis Philippe, Frédéric Augier, Pascal Fongarland. CFD modeling of mass transfer in Gas-Liquid-Solid catalytic reactors. *Chemical Engineering Science*, 2021, 233, pp.116378. 10.1016/j.ces.2020.116378 . hal-03150137

HAL Id: hal-03150137

<https://ifp.hal.science/hal-03150137>

Submitted on 23 Feb 2021

HAL is a multi-disciplinary open access archive for the deposit and dissemination of scientific research documents, whether they are published or not. The documents may come from teaching and research institutions in France or abroad, or from public or private research centers.

L'archive ouverte pluridisciplinaire **HAL**, est destinée au dépôt et à la diffusion de documents scientifiques de niveau recherche, publiés ou non, émanant des établissements d'enseignement et de recherche français ou étrangers, des laboratoires publics ou privés.

CFD modeling of mass transfer in Gas-Liquid-Solid catalytic reactors

Hanane Bouras^{1,2}, Yacine Haroun^{1,*}, Régis Philippe², Frédéric Augier¹, Pascal Fongarland²

1 : IFP Energies Nouvelles, Etablissement Lyon, Rond-Point Echangeur Solaize, F-69360
Solaize, France;

2 : Université de Lyon, CPE Lyon, Univ. Claude Bernard Lyon 1, CNRS, Laboratoire de Génie
des Procédés Catalytiques (UMR 5285), 43 bd du 11 novembre 1918, F-69616 Villeurbanne,
France.

Submitted to

Chemical Engineering Science

Corresponding Author: yacine.haroun@ifpen.fr

Tel.: +33 (0)4 37 70 29 29

22
23
24
25
26
27
28
29
30
31
32
33

34
35

36

37
38

39

40

41

42

Abstract

This work investigates Gas-Liquid-Solid mass transfer coupled to heterogeneous catalytic reaction using Computational Fluid Dynamics (CFD). The numerical model is based on the Volume-of-Fluid (VOF) approach, coupled with a convection-diffusion equation for mass transfer resolution. First, the numerical method was validated on a case of falling liquid film over a semi-infinite planar surface. Then, a micro-structured reactor with α -methylstyrene hydrogenation is studied. A good agreement is found between experimental data of (Tourvieille et al. 2013) and simulation results. Afterwards, a vertical spherical beads string is investigated. Convective transport by transversal velocities is identified as an important contributor to the overall Gas-Liquid-Solid mass transfer. While the film model is applicable in pure diffusion regimes, the resistances-in-series model is not relevant and over-estimates the real mass transfer by nearly 30% when mass transfer occurs in liquid film flow without bulk.

The present work shows how CFD can be an effective tool for predicting hydrodynamic and catalyst geometry effect on mass transfer in Gas-Liquid-Solid reactors.

Keywords: Gas-Liquid-Solid reactors; mass transfer; CFD; volume of fluid method; film model; catalytic reaction

43 **Nomenclature**

r_{Pd}	Intrinsic reaction rate	$[\text{mol}\cdot\text{s}^{-1}\cdot\text{g}_{Pd}^{-1}]$
a_{GL}	Gas-liquid specific interfacial area	$[\text{m}^2\cdot\text{m}_{Liq}^{-3}]$
a_{LS}	Liquid-solid specific interfacial area	$[\text{m}^2\cdot\text{m}_{Liq}^{-3}]$
A_{LS}	Liquid solid contact area	$[\text{m}^2]$
$A_{S,cata}$	Catalyst surface	$[\text{m}^2]$
C	Solute concentration	$[\text{mol}\cdot\text{m}^{-3}]$
C_{AMS}	Initial α -methylstyrene concentration	$[\text{mol}\cdot\text{m}^{-3}]$
C_{H_2}	Hydrogen concentration	$[\text{mol}\cdot\text{m}^{-3}]$
$C_{H_2}^*$	Hydrogen thermodynamic equilibrium concentration	$[\text{mol}\cdot\text{m}^{-3}]$
\overline{C}_{S,H_2}	Mean hydrogen surface concentration	$[\text{mol}\cdot\text{m}^{-3}]$
D	Diffusion coefficient	$[\text{m}^2\cdot\text{s}^{-1}]$
C	Solute concentration	$[\text{mol}\cdot\text{m}^{-3}]$
D_E	Effective diffusivity in the porous catalyst	$[\text{m}^2\cdot\text{s}^{-1}]$
D_{H_2}	Hydrogen molecular diffusion coefficient	$4.88\cdot 10^{-9} [\text{m}^2\cdot\text{s}^{-1}]$
\overline{Flux}	Hydrogen consumption flux	$[\text{mol}\cdot\text{s}^{-1}]$
\vec{g}	Gravity acceleration	$9.81 [\text{m}\cdot\text{s}^{-2}]$
k	Intrinsic reaction rate constant	$[\text{mol}^{0.27}\cdot\text{s}^{-1}\cdot\text{g}_{Pd}^{-0.27}]$
k_{GL}	Gas-liquid mass transfer coefficient	$[\text{m}\cdot\text{s}^{-1}]$
K_{GL}	Higbie gas-liquid mass transfer coefficient	$[\text{m}\cdot\text{s}^{-1}]$
k_{LS}	Liquid-solid mass transfer coefficient	$[\text{m}\cdot\text{s}^{-1}]$
K_{ov}	Overall external GLS mass transfer coefficient	$[\text{m}\cdot\text{s}^{-1}]$
$K_{ov,A}$	Analytical external overall mass transfer coefficient	$[\text{m}\cdot\text{s}^{-1}]$
$K_{ov,FM}$	overall external mass transfer coefficient by film model	$[\text{m}\cdot\text{s}^{-1}]$
$K'_{ov,FM}$	Modified overall external mass transfer coefficient by film model	$[\text{m}\cdot\text{s}^{-1}]$
K_R	Overall external mass transfer coefficient by resistances-in-series model	$[\text{m}\cdot\text{s}^{-1}]$
n	Reaction order	$0.73 [-]$
P	Operating pressure	$[\text{bar}]$
Q_L	Liquid flow rate	$[\text{m}^3\cdot\text{s}^{-1}]$
Re_i	Inlet Reynolds number of the i-th phase $Re_i = \rho_i v_i D_i / \mu_i$	$[-]$
Sh_{GLS}	Gas-liquid-solid Sherwood number $Sh_{GLS} = K_{ov} \delta_{geo} / D_{H_2}$	$[-]$
T	Operating temperature	$283 [\text{K}]$
$t_{contact}$	Contact time(in the Higbie approach)	$[\text{s}]$
\vec{u}	Velocity vector	$[\text{m}/\text{s}]$
V_{cata}	Catalyst volume	$[\text{m}^3]$
v_G	Local Gas phase velocity	$[\text{m}\cdot\text{s}^{-1}]$
v_i	Interface velocity	$[\text{m}\cdot\text{s}^{-1}]$
v_L	Local liquid phase velocity	$[\text{m}\cdot\text{s}^{-1}]$
V_{Liq}	Liquid volume	$[\text{m}^3]$
W_{Pd}	Palladium mass fraction in the catalyst	$[-]$
X_{AMS}	α -methylstyrene conversion	$[\%]$

44 **Greek letters**

α_L	Liquid volume fraction $\alpha_L = V_{liq} / V_{fluid}$	$[-]$
Φ	Level-set function	$[-]$
ρ_i	Density of phase i	$[\text{kg}\cdot\text{m}^{-3}]$

μ_i	Viscosity of phase i	[Pa.s]
σ	Surface tension	[N.m ⁻¹]
κ_i	Interface curvature	[-]
ρ_{cata}	Catalyst density	[kg.m ⁻³]
η_S	Surface efficiency factor	[-]
Φ_n	Thiele modulus	[-]
δ_{cata}	Catalyst layer thickness	[m]
β	Fully developed flow liquid film thickness	[m]
δ_{app}	Apparent liquid film thickness	[m]
δ_C	Liquid film thickness at the channel's centre	[m]
δ_A	Arithmetic mean liquid film thickness $\delta_A = \frac{1}{N} \sum_{i=1}^N \delta_i$	[m]
δ_{geo}	Geometric liquid film thickness $\delta_{geo} = V_{liq}/A_{LS}$	[m]
δ_H	Harmonic mean liquid film thickness $\delta_H = \frac{1}{N} \sum_{i=1}^N 1/\delta_i$	[m]

45 **Abbreviations**

<i>CLSVOF</i>	Coupled Level-Set and VOF
<i>VOF</i>	Volume Of Fluid
<i>LS</i>	Level-Set
<i>CICSAM</i>	Compressive Interface Capturing Scheme for Arbitrary Meshes
<i>UDS</i>	User Defined Scalar
<i>CFD</i>	Computational Fluid Dynamics
<i>GLS</i>	Gas-Liquid-Solid
Pd	Palladium

46 **1. Introduction**

47 Gas-liquid-solid reactors with a fixed bed are widely used in industry, they are encountered in
48 several applications such as petroleum refining, chemicals production, pharmaceuticals, waste-water
49 treatment, and many other fields. In most cases, the gas flows next to the liquid flowing around and
50 wetting totally or partially a solid phase (catalyst), these reactors operate in co-current down-flow or
51 up-flow configurations, as well as counter-current flow configuration. Regarding the widely
52 encountered case where the limiting reagent is initially contained in the gas phase, due to the solute
53 concentration gradients between phases, two interfacial gas-liquid and liquid-solid mass transfers
54 resistance could take place before allowing a reaction on the catalyst particles. These external
55 transfers can be merged as an overall gas-liquid-solid transfer coefficient. Reliable design of such
56 processes depends on the ability to accurately predict the hydrodynamics, the interfacial mass
57 transfer rates, and their couplings. However, the interfacial mass transfers are affected by

58 hydrodynamic parameter variations such as film thickness and velocity field distribution. In addition,
59 for the sake of simplicity, gas-liquid-solid mass transfer coefficients in such reactors are usually
60 estimated using (i) the resistances-in-series model or (ii) the film model. On one hand, the
61 resistances-in-series model was derived assuming a bulk concentration in the liquid phase. However,
62 in the specific case of co-current down-flow occurring in trickle bed or in falling film reactors, as the
63 liquid film thickness happens to be thin, the existence of a bulk concentration in the liquid phase is
64 far from being obvious and the applicability of this widely encountered approach needs to be
65 reviewed. On the other hand, the film model developed by Lewis and Whitman (1924) defines mass
66 transfer coefficients as the ratio of molecular diffusion coefficient to concentration boundary layer
67 thickness. However, the difficulty lies in the right estimation of mass transfer boundary layer
68 thickness in complex flows.

69 In recent years, Computational Fluid Dynamics (CFD) has proved to be a powerful tool for small
70 scales and local phenomena analysis which are difficult to investigate experimentally. CFD enable
71 access to velocity, pressure and concentration fields in complex systems and geometries through the
72 resolution of continuity, momentum and concentration transport equations respectively. Several
73 numerical works investigated the multiphase flow along solid surfaces, including mass transfer
74 restrained to gas-liquid interfacial transfer. (Haroun et al. 2010b) studied interfacial reactive mass
75 transfer in a 2D stable falling liquid film, using the Volume-Of-Fluid approach (VOF) to solve the film
76 hydrodynamics, and a modified concentration transport equation including the thermodynamic
77 equilibrium at the gas-liquid interface. The simulated Sherwood numbers were compared to the
78 analytical solution suggested by (Higbie 1935) and a good agreement was achieved. (Xu et al. 2008)
79 used the VOF method to study the gas-liquid interfacial mass transfer in a 2D wavy falling film, in
80 order to improve the understanding of the interface velocity fluctuations effect on gas-liquid mass
81 transfer, the results were compared to an empirical experimental expression. (Haroun et al. 2010a;
82 Haroun et al. 2012; Haroun and Raynal 2016) applied the numerical model developed in (Haroun et
83 al. 2010b) on a 2D structured packing element, to study the effect of geometry on liquid film flow

84 and mass transfer, a good agreement is found with (Higbie 1935) solution. (Marschall et al. 2012)
85 investigated the mass transfer for 3D free-surface flows, namely a stagnant liquid film and gas
86 bubble, using the VOF method and a modified concentration transport equation including Henry's
87 law, the comparison with analytical and experimental results shows a good agreement. Later on,
88 (Sebastia-Saez et al. 2013) evaluated the two-phase film flow and gas-liquid mass transfer along a
89 structured packing element, the results show a reasonably good agreement with theoretical and
90 experimental data, such as the liquid film thickness and Sherwood number. (Chii-Dong et al. 2011)
91 conducted 2D and 3D simulations of the two-phase flow inside a falling film micro-reactor, the
92 numerical model is based on the VOF approach, this preliminary study highlights the complexity to
93 predict flow behavior in micrometric high aspect ratio geometries, since convergence difficulties
94 were faced particularly for the interface stability. Despite the numerous scientific studies on two-
95 phase free-surface flow simulation and interfacial mass transfer, only few numerical studies
96 simulated the gas-liquid-solid mass transfer considering a heterogeneous catalytic reaction. The
97 majority of these works are based on the Eulerian framework, where the gas-liquid and liquid-solid
98 interfaces are not tracked explicitly. For instance, Lopes et al. (2007) and Lopes and Quinta-Ferreira
99 (2007) proposed a CFD model coupling hydrodynamics to catalytic wet air oxidation (CWAO) of
100 vanillic and phenolic acids respectively. The authors validated their CFD model against hydrodynamic
101 experimental data, before conducting predictive simulation of the reactive performance. In the same
102 context, Lopes and Quinta-Ferreira (2010) used both the Euler-Euler and VOF method to predict
103 reactive performance of CWAO. The numerical domain consisted of 200 non-overlapping spherical
104 particles. Because of coarse meshing resolution, the authors found better predictions using Euler-
105 Euler as opposed to VOF model. Later on, (Jejurkar et al. 2020) investigated the gas-liquid-solid mass
106 transfer in a trickle-bed reactor, the two-phase flow is modelled using an Euler-Euler model where
107 the gas-liquid and liquid-solid interfaces are not tracked explicitly. In summary, there are no
108 contributions on numerical investigation of gas-liquid-solid mass transfer coupled with
109 heterogeneous catalytic reaction using the VOF approach.

110 The aim of the present work is to use computational Fluid Dynamics to improve the understanding
111 of mass transfer in gas-liquid-solid contactors, when the transfer is accompanied by catalytic
112 heterogeneous reactions on the solid phase. The multiphase hydrodynamic resolution is based on
113 the Volume-Of-Fluid (VOF) numerical approach, while mass transfer resolution is investigated by a
114 convection-diffusion transport equation.

115 First, the CFD modeling is validated on a 2D laminar falling film with mass transfer along a vertical
116 semi-infinite catalyst plane by comparing the results to available models from the literature. The
117 model is then applied on a 3D falling film micro-structured reactor and pellet string reactor to couple
118 hydrodynamics, mass transfers and heterogeneous reaction. The modelling results are compared to
119 the experimental work of (Tourvieille et al. 2013), for α -methylstyrene catalytic hydrogenation in a
120 micro-structured reactor. For all the aforementioned cases, a particular attention is attributed to the
121 overall mass transfer calculation. The gas-liquid-solid overall mass transfer coefficient obtained by
122 CFD is compared to (i) the gas-liquid and liquid-solid resistances-in-series modeling and (ii) the one-
123 film mass transfer modeling. The results are further discussed and an adapted modeling methods
124 suggested.

125 Simulations of two phase flow are carried out with the volume of fluid method (VOF) with the
126 commercial CFD software ANSYS Fluent 19. In the following section, the governing equations are
127 described. Section 3 presents the model validation on a 2D falling liquid film over a vertical plane.
128 The results for a falling film micro-structured reactor and pellet string reactor are presented in
129 Section 4.

130 ***2. Computational model***

131 ***2.1. hydrodynamic model***

132 The present work aims to couple multiphase flow with gas-liquid-solid mass transfer and
133 reaction at the solid surface. To do so, the multiphase flow is solved using the volume of fluid

134 approach (VOF), which is a numerical method suitable to describe immiscible fluid flows by resolving
 135 the transport equation (1) of the volume fraction α in the computational domain.

$$\frac{\partial \alpha_L}{\partial t} + \vec{u} \cdot \nabla \alpha_L = 0 \quad (1)$$

136 Where α_L represents the liquid volume fraction ranging from 0 to 1. A value of 1 stands for
 137 liquid filled cells, whereas a value of 0 stands for gas filled cells. The interface is represented by the
 138 values in between. The VOF method tracks and describes explicitly the interface between the
 139 flowing fluids using interface reconstruction or finite volume discretization schemes.

140 The VOF approach might face limitations for complex flow configurations, such as high aspect
 141 ratio geometries, where spurious fluxes appear at the interface which becomes unstable. For this
 142 reason, the Coupled Level-Set (LS) and VOF (CLSVOF) method is used (Sussman and Puckett 2000).
 143 To begin with, the Level-Set method is a numerical scheme which deals with fluid-interface motion,
 144 usually used for an accurate resolution of the interface topology. The LS method solves the evolution
 145 of a level-set indicator function Φ as the following:

$$\frac{\partial \Phi}{\partial t} + \vec{u} \cdot \nabla \Phi = 0 \quad (2)$$

146 Where Φ is positive on one side of the interface, negative on the other side, and equal to zero at the
 147 interface. The LS formulation captures the interface with a higher accuracy than VOF but suffers
 148 from mass conservation issues. However, these issues are overcome by combining the LS and VOF
 149 methods (CLSVOF) (Sussman and Puckett 2000). In the scope of this work, CLSVOF is used when
 150 convergence issues or interface stability issues are encountered.

151 In addition, the conservation of mass (eq. (3)) and momentum equations (eq. (4)) are also
 152 solved for the gas-liquid incompressible and isothermal flow.

$$\nabla \cdot (\rho \vec{u}) = 0 \quad (3)$$

$$\rho \left(\frac{\partial \vec{u}}{\partial t} + \vec{u} \cdot \nabla \vec{u} \right) = -\nabla P + \mu \nabla^2 \vec{u} + \rho \vec{g} + \vec{F} \quad (4)$$

153 The force \vec{F} considered in equation (4) accounts for external body forces other than gravity,
154 pressure and viscosity. In this work, this force includes the effects of surface tension on the gas-
155 liquid and liquid-solid interfaces, it is modelled by the continuum surface force (CSF) model
156 proposed by (Brackbill et al. 1992) as the following :

$$F_{vol} = \sigma_{ij} \frac{\rho \kappa_i \nabla \alpha_i}{\frac{1}{2}(\rho_i + \rho_j)} \quad (5)$$

157 Where κ_i is the interface curvature, ρ_i is the density of phase i, ρ the volume-averaged density,
158 and σ_{ij} is the surface tension. The VOF model requires fine meshes for the gas-liquid interface to be
159 sharp, coarse meshes may induce errors in the interface curvature values, which may lead to
160 aberrant values of velocity, also known as spurious fluxes (Meier et al. 2002).

161 To guarantee resolution accuracy of the volume fraction transport equation, time step size
162 should fulfil the CFL condition (Courant-Friedrichs-Levy). This condition depends on the mesh and
163 velocity profile. As the velocity profile changes at each iteration, the variable time-step option was
164 used to ensure a maximum CFL value of 1.

165 The numerical simulations are performed using ANSYS Fluent v19.2, which is a commercial code.
166 The gas-liquid interface was advected using the Compressive Interface Capturing Scheme for
167 Arbitrary Meshes (CICSAM), the mass and momentum conservation equations were discretized using
168 the second order upwind numerical scheme, and the Coupled algorithm was used for the pressure-
169 velocity coupling.

170 **2.2. mass transfer model**

171 For multiphase flows, ANSYS Fluent allows solving an additional scalar transport equation in the
172 mixture, which is a User Defined Scalar (UDS) equation. To obtain the mass transfer coefficients
173 between the different phases, the limiting reagent concentration was computed inside the domain
174 using the latter approach as follows:

$$\frac{\partial C}{\partial t} + \nabla \cdot (uC - D\nabla C) = S \quad (6)$$

175 Where u is the velocity, C is the solute concentration inside the domain, D is the diffusion coefficient
 176 in (m^2/s) and S is a user defined source term.

177 This work investigates the gas-liquid-solid mass transfer in the presence of a heterogeneous catalytic
 178 reaction at the surface of the solid catalyst using two methods. The first one consists of simulating a
 179 gas absorption into the liquid, coupled to its consumption by a heterogeneous reaction at the solid
 180 surface. The second one is based on the resistances-in-series model, where the gas-liquid and liquid-
 181 solid mass transfer coefficients are estimated separately, to be used to estimate the overall mass
 182 transfer coefficient.

183 **2.3. Implementation of the heterogeneous catalytic reaction**

184 In many cases, the heterogeneous reaction takes place in the porous catalyst layer volume,
 185 through a coupled reaction/diffusion process. It can be modelled by the addition of a source term
 186 through this catalyst volume, meaning that the diffusion inside the catalyst needs to be taken into
 187 account, as well as an accurate description of the porous catalytic layer. Implementing a catalyst
 188 discretisation in the CFD calculation would impact significantly computation time. Therefore, in this
 189 work, the heterogeneous catalytic reaction is accounted for by a surface reaction modulated with a
 190 surface effectiveness factor η_s to take into account possible internal diffusion limitation. The
 191 following flux condition at the surface of the catalyst is derived.

$$Flux = - \frac{\eta_s \rho_{cata} W_{Pd} V_{cata} a_c}{A_{s,cata}} \quad (7)$$

192 Where a_c is the intrinsic reaction rate, W_{Pd} is the Pd mass fraction in the catalyst, V_{cata} and
 193 ρ_{cata} are respectively the catalyst volume and density, and η_s is the surface efficiency factor which
 194 is estimated classically through the Thiele modulus Φ_n . Since the flux condition (equation (7)) is
 195 applied at the catalyst's external surface, the concentration within the catalyst pores is not
 196 accessible. Smaller scale simulations are required to access such information. The α -methylstyrene

197 catalytic hydrogenation reaction was considered with a Pd/Al₂O₃ catalyst. Due to its very fast
 198 intrinsic kinetics, this reaction is very often operated in full external mass transfer regime and is a
 199 good candidate to probe chemically overall external mass transfer efficiency of different GLS reactor
 200 configurations (Meille et al. 2002; Meille and de Bellefon 2004). The reaction rate simplifies to an nth
 201 order reaction in the selected experimental conditions:

$$r_{Pd} = k C_{H_2}^n \quad (8)$$

202 Where $n = 0.73$ and k is the reaction rate constant (Tourvieille et al. 2013). As the reaction rate
 203 depends on hydrogen concentration, the concentration transport equation (eq. (6)) is solved for
 204 hydrogen only. The reaction is accounted for using the flux method explained above (eq. (7)).

205 Even though the flux condition is applied on the surface of the catalyst, the diffusion throughout
 206 the catalyst volume is accounted for by the efficiency factor, which is defined as the following for an
 207 nth order catalytic reaction and is estimated at each mesh cell:

$$\eta_S = \frac{1}{\Phi_n} = \sqrt{\delta_{cata}^2 \frac{(n+1)\rho_{cata}W_{Pd}kC_{H_2}^{n-1}}{2D_E}} \quad (9)$$

208 Where δ is the catalyst thickness, k is the reaction rate constant and D_E is the effective
 209 diffusivity. This latter parameter is estimated as $D_{H_2}/4$ since the tortuosity ranges from 2 to 3, and
 210 the internal porosity is nearly 0.6 (Tourvieille et al. 2013) and there is no Knudsen diffusion term.

211 Since the reaction rate and flux condition (eq. (7)) depend on the hydrogen concentration, only
 212 one concentration convection-diffusion equation is solved for H_2 concentration. The overall mass
 213 transfer coefficient can be post-processed after the solute concentration computation, the total
 214 hydrogen consumption flux is used to calculate the global mass transfer coefficient $K_{ov} \cdot a_{GL}$ and the
 215 AMS conversion X_{AMS} as follows directly linked to the 1:1 stoichiometry between the 2 reactants:

$$K_{ov} \cdot a_{GL} = \frac{\text{hydrogen consumption flux}}{V_{liq} (C_{H_2}^* - \bar{C}_{S_{H_2}})} \quad (10)$$

$$X_{AMS} = \frac{\text{hydrogen consumption flux}}{Q_L C_{AMS}} \quad (11)$$

216 a_{GL} is the gas-liquid interfacial area, V_{liq} is the liquid volume inside the reactor, C_{AMS} is the AMS
 217 concentration fixed to 1 mol/m³ at the inlet, Q_L is the liquid volumetric flow rate. The gas-liquid
 218 interfacial area a_{GL} has been chosen arbitrarily.

219 $C_{H_2}^*$ is the thermodynamic equilibrium concentration of H₂ in the liquid phase (mol/m³) given by the
 220 following expression (Herskowitz et al. 1978) :

$$C_{H_2}^* = 1.3 (0.0145.T(K) - 1.6985)P(bar) \quad (12)$$

221 Where T and P are the operating temperature and pressure.

222 \overline{C}_{sH_2} used in equation (10) is the mean hydrogen concentration at the catalyst's surface. Because
 223 of various possible definitions and for verification purpose, it was determined using two methods.
 224 The first one consists in calculating the average concentration at the catalyst surface at the post-
 225 processing stage of the CFD simulation. The second method is based on the hydrogen consumption
 226 flux at the catalyst surface. At the permanent regime, the hydrogen consumption flux is equivalent
 227 to the reactive flux at the catalyst surface, therefore the following model can be used to estimate
 228 \overline{C}_{sH_2} :

$$\begin{aligned} \overline{Flux} &= K_{ov} a_{GL} V_{liq} (C_{H_2}^* - \overline{C}_{sH_2}) \\ &= \sqrt{\delta_{cata}^2 \frac{(n+1)\rho_{cata} W_{Pd} k \overline{C}_{sH_2}^{-n-1}}{2D_E}} \cdot \frac{\rho_{cata} W_{Pd} V_{cata} k \overline{C}_{sH_2}^n}{A_{s,cata}} \end{aligned} \quad (13)$$

229 Where \overline{Flux} is the averaged hydrogen consumption flux at the catalyst surface. Equation (13) is a
 230 non-linear equation which can be solved using an optimization algorithm such as a Levenberg-
 231 Marquardt one. In this work, the two approaches lead to very similar results, as the hydrogen
 232 surface concentration estimated by both methods are close, therefore only the first method is finally
 233 used in the following sections.

234 **2.4. Resistances-in-series model analysis**

235 Gas Liquid Solid reactor models usually use the resistances-in-series model to estimate the
 236 overall mass transfer coefficient, termed $K_R a_{GL}$ to distinguish it from $K_{ov} a_{GL}$ presented in equation
 237 (10), considering that the overall external mass transfer inside such reactors is governed by two
 238 drivers in series, gas-liquid and liquid solid mass transfer resistances. First, a gaseous component
 239 diffuses from the gas bulk to the liquid film through the gas-liquid interface, the solute concentration
 240 stabilizes inside the liquid volume and reaches a liquid bulk concentration, then it is consumed by
 241 the heterogeneous reaction at the catalyst surface.

242 The overall mass transfer coefficient K_R is determined using the resistances-in-series model,
 243 defined as follows:

$$\frac{1}{K_R a_{GL}} = \frac{1}{k_{GL} a_{GL}} + \frac{1}{k_{LS} a_{LS}} \quad (14)$$

244 This model is developed assuming the presence of a liquid bulk inside the liquid film. The gas
 245 phase consists of pure H_2 , and as the hydrogen is poorly soluble in the liquid phase, the gas-liquid
 246 mass transfer coefficient represents the liquid-side mass transfer.

247 The mass transfer coefficients k_{GL} and k_{LS} are determined respectively from simulations of:

- 248 • Physical gas absorption into the liquid through the gas/liquid interface
- 249 • Physical solid dissolution into the liquid through the liquid/solid interface

250 First of all, the physical gas absorption mass transfer coefficient k_{GL} is obtained after solving
 251 equation (6), considering a zero-concentration flux at the catalyst surface. The solute diffuses
 252 throughout the gas-liquid interface and accumulates inside the liquid film. At steady state, equation (
 253 6) takes the following form:

$$\nabla \cdot (uC) = D \nabla^2 C \quad (15)$$

254 The convective flux difference (uC) between the inlet and the outlet of the domain is calculated to
 255 estimate the diffusion flux. The mass transfer coefficient is then defined from the diffusion flux as
 256 the following:

$$k_{GL} = \frac{D\nabla^2 C}{a_{GL}(C^* - C_B)} \quad (16)$$

257 Where C^* is the concentration at the interface, equal to the thermodynamic equilibrium
 258 concentration. Whereas C_B is the mean solute concentration in the liquid film.

259 In order to determine the mass transfer coefficient k_{LS} , the solid dissolution is simulated
 260 considering the diffusion properties of Hydrogen from the solid to the liquid. The concentration
 261 convection-diffusion equation (eq. (6)) is solved considering a zero-concentration flux at the gas-
 262 liquid interface. k_{LS} is calculated using the following equation:

$$k_{LS} = \frac{D\nabla^2 C}{a_{LS}(C_{wall} - C_B)} \quad (17)$$

263 Where C_{wall} is the concentration at the surface of the catalyst, and C_B is the mean solute
 264 concentration in the liquid film.

265 The coefficients k_{LS} and k_{GL} are then used to estimate the overall mass transfer coefficients using
 266 the resistances-in-series model presented in equation (14).

267 **3. Validation case**

268 **3.1. 2D simulation of mass transfer in a liquid falling film**

269 This section presents the simulations performed to develop and validate the numerical model. It
 270 consists of a 2D falling liquid film over a vertical plate, the aim is to guarantee a good agreement
 271 between the predictions and adequate analytical solutions, and to verify the validity of the
 272 resistances-in-series and film models in this numerical set-up.

273 **3.1.1. Set-up & boundary conditions**

274 The computational domain consists of a vertical plane plate of 1mmx250mm, water and
 275 hydrogen enter the domain at the top, and flow co-currently downward over the plate. The

276 hexahedral mesh has a high cell density near the plane plate in order to improve the interface
277 sharpness and concentration gradients in the liquid film

278 The boundary conditions are presented in Figure 1. The gas and liquid enter the domain at
279 $Re_G = 2.74$ and $Re_L = 3.98$ respectively. The concentration is fixed to the equilibrium
280 concentration C^* at the gas inlet and gas-adjacent wall, and to $C = 0$ at the liquid inlet. At the
281 remaining boundaries, Neumann boundary conditions ($\nabla C = 0$) are specified.

282 **3.1.2. Mesh convergence study**

283 In their work, Haroun et al. (2010b) recommended to have at least 5 cells in the concentration
284 boundary layer for an accurate concentration gradient description and gas-liquid mass transfer
285 calculation. In order to determine the adequate mesh resolution to obtain accurate numerical
286 description of hydrodynamics and overall gas-liquid-solid mass transfer, a mesh sensitivity study is
287 performed. All the tested meshes are structured, for which the mesh resolutions are varied as
288 shown in Figure 2. The criterion on which the final mesh is selected is mesh convergence calculation
289 of the overall Sherwood number.

290 Figure 2 shows the evolution of gas-liquid-solid Sherwood number with mesh resolution. It can be
291 observed that the overall Sherwood number does not change for meshes above $4.7 \cdot 10^5$ cells,
292 corresponding to 14 cells within the liquid film thickness, indicating the mesh convergence of the
293 simulation. It is interesting to note that the mesh used in this work are hexahedral with higher cell
294 resolution near the catalyst surface in order to improve the interface sharpness and the
295 concentration gradients calculation.

296 It is to be noted that for the other study cases : 3D Falling Film Micro-Reactor and 3D falling film on
297 spherical particles were meshed with mesh resolution much higher than 14 mesh cells within the
298 liquid film. Moreover, it is interesting to note that in the Falling Film Micro-Reactor, a very sharp

299 mesh with a mesh resolution higher than the requirement of 14 cells is used in order to capture the
300 film's meniscus shape.

301 **3.1.3. Analytical solution**

302 The liquid flow over such a semi-infinite vertical plane plate was studied by (Nusselt 1916), who
303 suggested an analytical expression for the interface velocity (u_I) and liquid film thickness (β)
304 depending on the flow and physico-chemical properties. The analytical solutions are expressed as
305 follows:

$$u_I = \frac{\rho_L g \beta^2}{2\mu_L} \quad (18)$$

$$\beta = \left(\frac{3\nu^2 Re_L}{g} \right)^{\frac{1}{3}} \quad (19)$$

306 Where β is the liquid film thickness. This analytical solution was used to validate the numerical
307 hydrodynamic results.

308 Concerning mass transfer validation, (Higbie 1935) developed a model to obtain the local and
309 global gas-liquid mass transfer coefficients in such films under laminar flow depending on the
310 contact time, the coefficients are expressed as follows:

$$k_{GL,local} = \sqrt{\frac{D}{\pi t_{contact}}} \quad ; \quad K_{GL} = 2 \sqrt{\frac{D}{\pi t_{contact}}} \quad ; \quad t_{contact} = \frac{l(x)}{u_I} \quad (20)$$

311 The contact time is estimated based on the interface curvilinear length $l(x)$ from the inlet to a
312 position x .

313 **Figure 3** shows the gas volume fraction distribution. It can be seen that the liquid film flows
314 continuously over the plane plate, this film seems to have a constant thickness. The liquid film is
315 slightly curved at the establishment zone near the inlet because the inflow velocity value is low.

316 The interface velocity and the liquid film thickness were compared to the analytical solution. As one
317 can see from the Table 2, the numerical values are in good agreement with the analytical values with

318 very low relative deviation for both evaluated parameters. When the flow is established, the
319 simulated liquid film maintains a constant thickness throughout the domain, the liquid film thickness
320 reported in Table 2 corresponds to the converged film thickness.

321 **3.1.4. Mass transfer validation**

322 **Figure 4** shows a comparison between the analytical and numerical local mass transfer
323 coefficients, for the 2D falling film over a vertical solid plate. The numerical mass transfer coefficient
324 k_{GL} is obtained using equation (16), where the bulk concentration C_B is taken at the furthest
325 location from the gas-liquid interface, at the solid surface. As one can see, there is a high difference
326 between the simulated and analytical values at the inlet of the domain, due to the difference
327 between concentration boundary conditions at adjacent gas and liquid inlets, causing a high
328 concentration gradient therein. However, overall, the numerical model reproduces the analytical
329 solution with a good agreement in the rest of the domain.

330 The gas-liquid mass transfer coefficient is well predicted by CFD simulations as seen above.
331 Similarly, considering the dissolution of chemical species from a solid surface into the liquid film, and
332 following the method described in the section 2.4, the liquid-solid mass transfer coefficient can be
333 computed. The diffusive flux is determined by Fick's law, considering the diffusion coefficient of
334 hydrogen.

335 The H_2 concentration profile in the liquid film when H_2 is consumed at the solid surface is
336 represented in **Figure 5**. As one can see, the obtained profile is linear within the liquid film, which
337 means that mass transfer takes place in the absence of a liquid bulk and due to the specific kinetics
338 (zeroth order in substrate) and gas conditions (pure and isobaric H_2 flow) this profile remains the
339 same all along the falling length. The corresponding overall mass transfer coefficient K_{ov} obtained
340 through equation(10), for this reactive simulation is of $5.99 \cdot 10^{-5} \text{ m.s}^{-1}$. It can be compared to K_R , its
341 physical counterpart obtained following the resistance in series strategy (eq. (14)). In K_R , the gas-

342 liquid and liquid-solid mass transfer resistances were obtained from the physical absorption and
 343 dissolution cases respectively, K_R is equal to $7.95 \cdot 10^{-5} \text{m} \cdot \text{s}^{-1}$. The results show a 27% deviation, as the
 344 resistances-in-series model overestimates the mass transfer coefficient. This deviation is due to the
 345 absence of a bulk concentration in the liquid film, as the film thickness is low and the flow is laminar
 346 and unidirectional, meaning that the radial mixing is poor.

347 K_{ov} was also compared to the analytical overall coefficient $K_{ov,A}$ obtained from the equations
 348 below for a similar situation but under pure diffusion only (no fluid convection), at steady state:

$$\left\{ \begin{array}{l} D_{H_2} \cdot \frac{dC_{H_2}}{dy} = 0 \\ D_{H_2} \nabla C_{H_2} \Big|_{y=0} = \frac{Flux}{A_{S,cata}} \quad \text{at } y = 0 \text{ (catalyst surface)} \\ C_{H_2}(y = y_I) = C_{H_2}^* \quad \text{at } y = y_I \text{ (gas - liquid interface)} \end{array} \right. \quad (21)$$

349 Where $Flux$ is the heterogeneous catalytic flux condition at the catalyst surface defined in equation
 350 (7), and $C_{H_2}^*$ is the hydrogen equilibrium concentration given by equation (12). The corresponding
 351 analytical concentration profile is given by the following expression:

$$C_{H_2}(y) = \frac{Flux}{D_{H_2}}(y - y_I) + C_{H_2}^* \quad (22)$$

352 The corresponding analytical overall mass transfer coefficient $K_{ov,A}$ is derived from equation (23
 353), and is expressed as the following:

$$K_{ov,A} \cdot a_{GL} = \frac{D_{H_2} \frac{dC_{H_2}}{dy}}{V_{liq}(C_{H_2}^* - C_{H_2,S})} = \frac{Flux}{V_{liq}(C_{H_2}^* - C_{H_2,S})} \quad (23)$$

354 This $K_{ov,A}$ and the overall mass transfer coefficient K_{ov} obtained by CFD are equal, indicating
 355 that in this configuration, the vertical convective down-flow does not impact the radial transport
 356 which is ensured only by pure diffusion in the liquid film thickness.

357 Similarly, the $K_{ov,FM} = D_{H_2}/\delta_{film}$ given by the film model gave a good agreement with the
 358 computed overall mass transfer coefficient K_{ov} , the relative deviation being equal to 1.3% as

359 reported in Table 3. This means that the diffusion layer thickness is nearly equal to the actual overall
360 hydrodynamic liquid film thickness.

361 **4. Study cases**

362 **4.1. 3D simulation of a Falling Film Micro-Reactor (FFMR)**

363 The developed numerical model has been applied to simulate one channel of a falling film micro-
364 structured reactor in order to validate its ability to predict hydrodynamic and mass transfer
365 parameters in a more complex set-up, where the liquid film thickness takes different values
366 depending on the location within the channel. This feature is obtained due to the structuration at
367 the sub-millimetre-scale of the channel, thus involving a flow driven by capillary and viscous forces.
368 The purpose is to improve the understanding of mass transfer behaviour in similar film
369 morphologies, to identify the most suitable mechanism to describe GLS mass transfer, and to
370 compare the numerical results with available experimental results published by (Tourvieille et al.
371 2013) on the hydrogenation of α -methylstyrene with a coated Pd/Al₂O₃ catalyst under mass transfer
372 controlled regime but also on liquid film profiles established by fluorescent confocal microscopy
373 under various flow conditions. These results were used to further validate the model both for
374 hydrodynamic and mass transfer predictions.

375 The FFMR (Large version) is a falling film containing several parallel micro-structured channels,
376 where the gas and liquid flow counter-currently, transferring the reagents from gas to the liquid and
377 from the liquid to the solid, in the case of the presence of a coated heterogeneous catalyst. Micro-
378 structuration applied to falling film contact mode brings very stable G-L interfaces and intensification
379 through liquid film thinning due to capillary forces. More details about the reactor can be found in
380 (Tourvieille et al. 2013) and in (Vankayala et al.).

381 Only one longitudinal half of a single channel has been simulated to reduce computation time, using
382 a symmetry boundary condition in the middle of the channel.

383 As in the experimental work where two different plates were used, two numerical domains were
384 considered: a first one without catalyst coating for the hydrodynamic validation, and a second one
385 taking into account the catalyst layer thickness of $40\mu\text{m}$.

386 As we assume that all the channels have an equivalent behaviour, the liquid is evenly distributed
387 at the inlet, all the liquid channels have the same liquid and gas flow rates (Tourvieille 2014).
388 Moreover, liquid enters the domain at $C_{H_2} = 0$, and the concentration of hydrogen in the gas phase
389 is constant for it consists of pure H_2 , and the interface H_2 concentration is equal to the equilibrium
390 concentration given by equation (12).

391 To be fully representative of the experimental work, and because starting procedure plays a
392 significant role on wetting, the channel is initially overflowed with the liquid at the inlet liquid
393 velocity. The contact angle was not characterized experimentally, thus different contact angle values
394 were tested in the model, and it is found that the liquid film profile is well represented with contact
395 angle values of 20° .

396 Liquid flow over a flat plane can take several forms. At large liquid flow rates, a continuous liquid
397 sheet is formed on the solid surface, which might breakup at certain locations. Falling film micro-
398 reactors are known for preventing film breakup, they facilitate the stability of the liquid film and the
399 corresponding gas-liquid interface and gas-liquid-solid 3-phase contact lines. Due to the combination
400 of capillary forces and small channel widths, liquid is pulled up along the sides of the channels and
401 covers up a significant portion of the channel width. The most desirable flow configuration is when
402 the liquid flows in a meniscus shape as shown in **Figure 6**, that is to say for small Weber numbers, as
403 the interface shape is governed by the interfacial energy.

404 Downward co-current two-phase flows were simulated, and converged liquid film profiles were
405 compared to the corresponding experimental results. In order to avoid compatibility issues between
406 the liquid phase and solid material of the FFMR, the hydrodynamic experiments were performed
407 using ethanol/hydrogen instead of MCH+AMS/hydrogen. For consistency purposes, hydrodynamic
408 simulations are performed using ethanol/hydrogen, and reactive mass transfer simulations are
409 carried out with MCH+AMS/hydrogen. The properties of ethanol/hydrogen are given in Table 1.
410 **Figure 6** shows this comparison for different inlet liquid flow rates. The numerical results are in good
411 agreement with the experimental values indicating a very good prediction of the hydrodynamics by
412 the CFD simulations.

413 The gas-liquid interface curves upwards moving from the channel's centre to the three-phase
414 contact lines (always located at the edges of the channel due to the starting wetting procedure), and
415 the interface is not disrupted across the numerical domain. The more the liquid flow rate increases,
416 the flatter the interface becomes. Such behaviour was found in many experimental studies
417 (Tourvieille et al. 2013; Yeong et al. 2006). Besides, the liquid film is contained inside the channel
418 regardless of tested liquid inlet flow rates in the investigated flow rate range. The results shown in
419 **Figure 7** were obtained with a contact angle value of 20°.

420 Logically, as shown in **Figure 7**, the corresponding specific gas-liquid area values are in good
421 agreement with the experimental results, with a relative deviation to the experimental results only
422 up to 10% at the lowest liquid flow rate. The variation of the specific gas-liquid area illustrates well
423 the effect of liquid flow rate, as this latter increases, the interface flattens, the mean liquid thickness
424 increases too leading to the decrease of the specific area.

425 **4.1.1. Mass transfer**

426 In this section, the two-phase flow of hydrogen and methylcyclohexane/ α -methylstyrene
427 mixture is investigated, and two channel dimensions were simulated for further validation. The
428 coated channels characteristics are summarized in **Table 4**.

429 As one can see from **Figure 8**, H_2 diffuses from the gas phase to the liquid phase, and is
430 consumed by the heterogeneous catalytic reaction at the solid wall. Due to the liquid film thickness
431 variation inside the channel, the liquid is saturated with H_2 near the three phase contact line as the
432 liquid film thickness is lower at this location. Whereas, at the channel's centre, the liquid film
433 thickness reached its maximum value leading to a lower H_2 concentration at the catalyst surface. In
434 addition, the mass transfer fully developed regime is reached at 5mm from the channel's inlet, thus
435 the concentration profile is the same at different plane cuts of the channel as shown in **Figure 8**.

436 Experimental liquid volumes were estimated using a developed correlation in (Tourvieille et al.
437 2013), which can explain the 20% difference between numerical and experimental liquid volumes
438 reported in **Table 5**.

439 As one can see from **Table 5**, the experimental and CFD predicted H_2 consumption fluxes are in
440 the same orders of magnitude and follow the same evolution with liquid flow rate. The relative
441 deviation between CFD and experimental results are 17%, 2% and 0.8% at liquid flow rates of
442 3ml/min, 5ml/min and 7ml/min respectively. The same findings apply on the α -methylstyrene
443 conversions. However, the overall mass transfer coefficients $K_{ov}a_{GL}$ show significant deviations
444 between experimental values and numerical values, this is mainly due to experimental liquid
445 volumes estimations. According to (Tourvieille et al. 2013), evaporation was noticed at low pressure
446 in the experiment and a significant liquid volume was found at the gas outlet. Thus, the effective
447 liquid volume inside the reactor in reaction conditions was lower than the one predicted through the
448 correlation and the overall mass transfer coefficients were overestimated. However, evaporation

449 was negligible at 5 bar, which means that data measured at 5 bar are the most reliable ones,
450 especially concerning the H₂ consumption flux (Tourvieille et al. 2013).

451 The deviation in $K_{ov}a_{GL}$ even for the best experiment remains large because of an important
452 difference in the liquid volume determination as already mentioned. For the experimental results, it
453 is approached through a correlation and for this work it is precisely simulated using the
454 hydrodynamic model. That's why in the following, comparisons with experimental data will be
455 carried out on the H₂ consumption flux (which is equivalent to a comparison in $K_{ov}a_{GL}V_{liq}$).

456 **Figure 9** compares experimental and numerical $K_{ov}a_{GL}V_{liq}$, as well as the evolution with liquid
457 flow rate and pressure for the 2 plates with different channel geometries. The quantity $K_{ov}a_{GL}V_{liq}$ is
458 equivalent to H₂ consumption flux normalized by the concentration difference between $C_{H_2}^*$ and the
459 surface concentration $C_{H_2,S}$. The computed $K_{ov}a_{GL}V_{liq}$ are very close to the experimental values
460 except at the minimum liquid flow rate where a more significant deviation is present, this might be
461 explained by a higher variability in the experiment. As one can see, the other numerical values are
462 within 10% around the experimental ones, this allows us to conclude that CFD was able to capture
463 and predict the effect of channel dimension on this coupled situation involving hydrodynamics, mass
464 transfer and heterogeneous reaction. One interesting fact, both numerical and experimental mass
465 transfer coefficients reach higher values with bigger channels which is counterintuitive in micro-
466 structuration. Indeed, micro-structuration is needed to obtain a curved and thinned liquid interface
467 in comparison to unstructured conventional falling films. However, because of the presence of the
468 free interface, too much structuration can be detrimental in this case, leading to thicker films with
469 the smaller channels at the same mean flow velocity or flowrate. This holds true as long as the 3-
470 phase contact lines remain stable and at the edges of the channels.

471 **Figure 10** shows a comparison between experimental and predicted values for α -methylstyrene
472 conversion at P=5bar. As one can see, numerical predictions are in good agreement with

473 experimental values thus validating the developed CFD model, the liquid flow rate effect on
474 conversion is also well represented.

475 The resistances-in-series model has been tested on this case study as well. The results are
476 summarized in Table 6. They show on average 32% deviation between the computed overall mass
477 transfer coefficients, $K_{ov}a_{GL}$, and the resistances-in-series model, K_Ra_{GL} . These results show that
478 the resistances-in-series model is not adapted to describe the overall mass transfer coefficient, the
479 liquid film thicknesses obtained in FFMRs are low, leading to the absence of a bulk concentration
480 within the liquid film.

481 Similarly to the semi-infinite planar case, the applicability of the film model was tested. An
482 interesting difference lies in the definition of the correct characteristic length because of the
483 encountered variable thickness in the cross section of it. Thus, different liquid film thicknesses were
484 used to define the film model mass transfer coefficient, namely the liquid thickness at the centre of
485 the channel δ_c , the arithmetic mean thickness δ_A , the geometric liquid thickness δ_{geo} defined as the
486 ratio of the liquid volume to the wetted surface, and finally the harmonic mean thickness δ_H .

487 The film model underestimates the mass transfer coefficient using δ_c , δ_A and δ_{geo} , and strongly
488 overestimates it using δ_H ; the lowest mean relative deviation reported in Table 7 for $K_{ov,FM}$
489 corresponds to the arithmetic mean liquid film thickness δ_A , the mean relative deviation is above
490 30% for the remaining liquid film thickness definitions. These differences are caused by the liquid
491 film morphology, where the film thickness is very low near the three-phase contact line and reaches
492 a maximum at the centre of the channel, causing important local differences in H_2 consumption at
493 these locations. Nonetheless, to reconcile the sophisticated CFD simulations with the simple film
494 model, a correction factor A can be introduced to the film model to predict well the mass transfer:

$$K'_{ov,FM} = A \frac{D}{\delta} \quad (24)$$

495 The results are presented also in Table 7 and the best fit was obtained using δ_A . However, δ_{geo} is
496 considered to be the most interesting thickness value, for its easier acquisition both experimentally
497 and numerically.

498 **4.2. 3D simulation of a reactive falling film on string of spherical** 499 **catalyst particles**

500 The previously studied cases consisted of falling films over a regular plane or micro-channel. In
501 order to highlight the effect of the solid catalyst shape and to go towards more complex geometries
502 encountered in fixed beds, simulations of reactive two-phase flow over stacked 1mm diameter
503 spheres were carried out. The purpose of this case study is to investigate the effect of liquid film
504 thickness distribution within the domain on GLS mass transfer involving a heterogeneous catalytic
505 reaction, and to check the validity of resistances-in-series and film models on a such complex
506 configuration. Contrary to the two previous cases, here the chosen geometry is likely to induce
507 convection in other directions than the main flow direction and its impact on overall external
508 transport from the gas phase to the solid catalyst surface will be investigated.

509 The three dimensional simulation domain consists of 12 spheres of 1mm diameter stacked inside
510 a cylinder, where the co-current hydrogen/water flow takes place by gravity from inlet to outlet. The
511 mesh was generated using SnappyHexMesh, with high refinement near the spheres to increase the
512 number of cells in the liquid film.

513 For the first hydrodynamic investigation, the gas and liquid inlet Reynolds numbers are 25 and
514 30 respectively, and the flow takes place in isothermal (T=283K) and isobaric conditions. The
515 hydrogen concentration at the liquid inlet is equal to zero, and C^* at the gas inlet, it is homogeneous
516 in the gas phase as it consists of pure hydrogen, and reaches the equilibrium concentration given by
517 equation (12) at the gas-liquid interface.

518 The liquid forms a continuous film over the catalyst particle string at steady state as shown in

519 **Figure 11-a**, the thickness varies throughout the domain. As one can see from **Figure 12-a**, the liquid
520 film is thinner at the equatorial plane of each particle and accumulates at the contact region
521 between spheres. Similarly, as shown in

522 **Figure 11-b** and **Figure 12-b**, the interface velocity reaches its maximum value where the liquid film
523 is thin and vice-versa, due to mass conservation inside the computational domain. The total number
524 of spheres was chosen in order to ensure the fully developed regime is reached.

525 **4.2.1. Mass transfer analysis**

526 The convection diffusion equation of concentration (eq. (6)) was solved at different pressure
527 conditions, that is to say at different thermodynamic equilibrium concentrations $C_{H_2}^*$. In order to
528 investigate the effect of particle shape on mass transfer, purely diffusive conditions are also
529 considered. The pure diffusion is an artificial calculation since the convective term is artificially
530 considered equal to zero in the concentration transport equation, but the liquid film thickness
531 profile remains the same as for convection-diffusion conditions.

532 As one can see from **Figure 13**, when convection is neglected in transport analysis, the diffusion
533 boundary layer is equivalent to the whole liquid film thickness (**Figure 13-a**). Whereas when the
534 convection effects are taken into account, the diffusion boundary layer is closer to the particles
535 (**Figure 13-b**), the liquid film is loaded with hydrogen since the concentration is maximum in a large
536 proportion of the liquid film, the concentration then decreases near the surface of the spheres
537 where it is consumed by the heterogeneous catalytic reaction.

538 In order to bring out the effect of convection, **Figure 14-a** compares the concentration profiles in
539 the liquid film at the great circle of a particle. As one can notice, the concentration profile is linear
540 when convection is neglected. In contrast, the convection boosts the solute transfer since the
541 concentration is nearly constant far from the spheres, and the diffusion is predominant near the
542 spheres as the concentration profile becomes linear.

543 **Figure 14-b** shows a comparison between the hydrogen consumption flux with and without
544 convection. The flux is significantly increased by convection in comparison to pure diffusion, it is on
545 average 6 times higher. This result is substantially different from the two previous study cases for
546 the radial velocity profile contributes to radial transport enhancement in this case. In addition, one
547 can also notice that the flux profile shape is smooth for pure diffusion and reaches peaks at the great
548 circle of particles. In contrast, when convection is considered, the flux profile shape is asymmetric
549 and reaches a peak at the top of each particle, following the shape of the radial velocity as shown in
550 **Figure 15**.

551 The same evolution is noticed for the distribution of the solute surface concentration on the
552 spheres surface. **Figure 16** shows the difference in surface concentration of the solute with and
553 without convection on the 10th sphere. For pure diffusion, the surface concentration is symmetric,
554 whereas the radial velocity boosts the concentration at the first hemisphere of the particles when
555 convective transport is considered.

556 The local overall external mass transfer K_{ov} obtained for convection-diffusion is represented in
557 **Figure 17**. K_{ov} is calculated at each mesh cell of the gas-liquid interface, and defined as the ratio of the
558 local hydrogen consumption flux and the local concentration difference $(C_{H_2}^* - \overline{C_{S,H_2}})$. K_{ov} follows
559 the same trend as the surface hydrogen consumption flux and surface concentration, **Figure 17**
560 reports only the data at P=1bar because the K_{ov} profiles are exactly the same for P=3bar and
561 P=5bar. After going through the flow stabilization zone at the inlet, for the 2-4 first spheres, the
562 mass transfer coefficient profile becomes similar from one sphere to another and is maximized at
563 the first hemisphere of each particle, with the liquid acceleration, then decreases at the second
564 hemisphere with the liquid deceleration.

565 The average external overall mass transfer coefficients are obtained by integrating the local
566 overall external mass transfer coefficient presented in **Figure 17** throughout one sphere in the fully
567 developed mass transfer regime, that is to say on the 10th sphere for instance. As done previously,

568 the apparent diffusion layer thickness is obtained from the average K_{ov} using the film model. The
569 apparent diffusion layer thicknesses reported in Table 8. The results show that the radial convection
570 enhances mass transfer. The apparent diffusion layer is low when convection is accounted for, this
571 means that the diffusion takes place in a small liquid film thickness near the surface, which was
572 explicitly noticed in Figure 14-a.

573 As shown in Table 8, The mass transfer coefficients determined by resistances-in-series model
574 are on average 37% higher than the obtained overall mass transfer coefficient, once again because
575 the gas-liquid and liquid-solid mass transfer layers overlap, since there is no bulk concentration in
576 the liquid film.

577 Concerning the film model, neither the geometric thickness nor the average thickness gives good
578 results, as the apparent diffusion layer thickness δ_{app} is very small compared to the liquid
579 hydrodynamic thickness.

580 Further investigation of the convection effect on mass transfer has been made, considering
581 several liquid Reynolds number conditions to investigate the liquid velocity and viscosity effects, the
582 diffusion coefficient remains fixed at $4.88 \cdot 10^{-9} \text{m}^2/\text{s}$. As one can see from Figure 18-a, the geometric
583 thickness increases with Reynolds number as well as viscosity.

584 The overall mass transfer coefficient is represented in Figure 18-b since the liquid film thickness
585 increases with the Reynolds number, the mean mass transfer layer becomes thicker and the mass
586 transfer coefficient decreases. However, convection enhances mass transfer since the convective
587 mass transfer coefficient remains higher than the purely diffusive mass transfer coefficient.

588 In order to gather all these data in a single correlation, a gas-liquid-solid Sherwood number
589 Sh_{GLS} corresponding to the overall external mass transfer has been estimated. Figure 19 shows that
590 this Sherwood number increases with the Reynolds number, and seems to reach an asymptotic value
591 of 6 in the investigated conditions since the flow regime is laminar. When the convection is

592 neglected, the mass transfer coefficient was equal to D/δ_{geo} , leading to a Sherwood number equal
593 to 1. Thus, a tentative correlation has been derived for this overall Sherwood number, taking the
594 following form:

$$Sh_{GLS} = Sh_{asymptotic} - (Sh_{asymptotic} - Sh_{diff}) \cdot \exp(-A \cdot Re) \quad (25)$$

595 Where Sh_{diff} is the Sherwood number for pure diffusion and $Sh_{asymptotic}$ is the asymptotic
596 value of the Sherwood number equal to 6 in this case. The constant A was fitted on the obtained
597 numerical data, and the tentative correlation is given by:

$$Sh_{GLS} = 6 - 5 \cdot \exp(-0.048 \cdot Re) \quad (26)$$

598 As one can see from **Figure 19**, Sherwood numbers estimated by the correlation presented in
599 equation (26) and by CFD are close, the maximum relative error is 11% and the average relative
600 error is 4.74%.

601 In summary, This case illustrates the effect of a more complex geometry corresponding to pellet
602 string reactor on hydrodynamic and mass transfer performances. It is found that the convection
603 enhances drastically the mass transfer rate, in contrast with the two previous study cases where
604 diffusion was the exclusive radial transport phenomenon. However, since the string of few particles
605 are stacked in a perfectly aligned pattern, the two-phase flow behavior is different from the one
606 encountered in trickle-bed reactors, where the catalyst particles are stacked randomly and are more
607 packed, leading to more complex phase distributions inside the reactor. Nevertheless, this work
608 shows that CFD simulation allows investigating realistic complex reactive systems such as trickle-bed
609 reactors.

610 **5. Conclusion**

611 A numerical model has been developed in order to improve the understanding of reactive falling
612 liquid films flow over different catalytic surfaces. This model coupled a robust hydrodynamic VOF

613 description with a consistent gas-liquid-solid mass transfer and a surface heterogeneous catalytic
614 reaction. Three case studies have been simulated, namely a 2D semi-infinite falling liquid film over a
615 vertical planar surface, a 3D falling film micro-reactor and a 3D falling liquid film over a string of
616 spherical particles.

617 First, the CFD modeling of two-phase flow in bidirectional domain and three dimensional micro-
618 channel reactor have been investigated. The simulation results were compared respectively to
619 Nusselt's model (Nusselt 1916) and experimental data of (Tourvieille et al. 2013). The simulation
620 results show a very good agreement in both cases.

621 Regarding mass transfer, the overall external gas-liquid-solid mass transfer behavior
622 encountered under heterogeneous catalytic reaction conditions is significantly different in the three
623 study cases. Indeed, For the 2D semi-infinite plate, the gas-liquid mass transfer coefficients is found
624 to be in good agreement with the analytical solution of (Higbie 1935). In addition, the gas-liquid-solid
625 mass transfer is well described by the film model, when a pure radial diffusion regime is reached at
626 steady state. Moreover, this work shows that the resistances-in-series model is not suitable to
627 describe mass transfer for this case, since it overestimates the mass transfer coefficient by 27%.

628 Regarding the 3D falling film micro-reactor (FFMR), a good agreement is obtained between
629 experimental and simulated overall mass transfer coefficients. It is found that the gas-liquid-solid
630 mass transfer is predominantly diffusive, a correction factor is proposed and introduced to the film
631 model to account for the non-uniform liquid film thickness in the channel. For FFMR system, it is also
632 found that the resistances-in-series model overestimates the overall mass transfer coefficient by
633 32% for similar aforementioned reasons as the 2D falling liquid film.

634 Finally, using the validated CFD model, mass transfer in trickling flow conditions over a string of
635 12 spherical catalyst particles with a heterogeneous catalytic reaction at the catalyst surface has
636 been studied, using the validated CFD model. It is found that the gas-liquid-solid mass transfer

637 regime is mainly dominated by the convection induced radially by this geometry. The convection
638 enhances mass transfer, leading to thin mass transfer boundary layers. In addition, it is found that
639 the film model does not give representative results for this case, and a new Sherwood number
640 correlation is developed to correct the model. This work shows also that the overall GLS external
641 mass transfer coefficients estimated by the resistances-in-series model are on average
642 overestimated by 37% again because of bulk concentration absence.

643 To conclude, this work shows that the mass transfer in two-phase laminar flows with reaction
644 occurring at the solid surface are dependent on the solid geometry and behave differently regarding
645 the overall external mass transfer. Not all the cases are equivalent to a simple falling liquid film, thus
646 each case needs to be studied separately. In addition, this work proves that CFD can be an a
647 powerful tool, not only to predict complex flow patterns, but also to simulate physically relevant
648 mass transfer processes coupled with heterogeneous reactions, as well as to improve the
649 understanding of multi-physics phenomena in gas-liquid-solid fixed bed reactors. Nowadays , thanks
650 to the development of high performance calculations resources, this approach might be extended to
651 fixed-bed reactors. However, the predictions would be limited to a few hundreds of particles instead
652 of the entire reactor. Even though the simulated scales are far from the reactor scale, the presented
653 numerical model can be applied to improve understanding of local mass transfer mechanisms.

654 *Publication bibliography*

655 Brackbill; J. U.; Kothe; D. B.; Zemach; C. (1992): A Continuum Method for Modeling Surface Tension.
656 In *Journal of Computational Physics* 100, pp. 335–354.

657 Chii-Dong, H.; Chang, H.; Chen, H. J.; Chang, C. L.; Li, H. H.; Chang, Y. Y. (2011): CFD simulation of the
658 two-phase flow for a falling film microreactor. In *International Journal of Heat and Mass Transfer* 54
659 (15-16), pp. 3740–3748. DOI: 10.1016/j.ijheatmasstransfer.2011.03.015.

660 Haroun, Y.; Legendre, D.; Raynal, L. (2010a): Direct numerical simulation of reactive absorption in
661 gas–liquid flow on structured packing using interface capturing method. In *Chemical Engineering*
662 *Science* 65 (1), pp. 351–356. DOI: 10.1016/j.ces.2009.07.018.

663 Haroun, Y.; Legendre, D.; Raynal, L. (2010b): Volume of fluid method for interfacial reactive mass
664 transfer: Application to stable liquid film. In *Chemical Engineering Science* 65 (10), pp. 2896–2909.
665 DOI: 10.1016/j.ces.2010.01.012.

666 Haroun, Y.; Raynal, L. (2016): Use of Computational Fluid Dynamics for Absorption Packed Column
667 Design. In *Oil Gas Sci. Technol.* 71 (3), p. 43. DOI: 10.2516/ogst/2015027.

668 Haroun, Y.; Raynal, L.; Legendre, D. (2012): Mass transfer and liquid hold-up determination in
669 structured packing by CFD. In *Chemical Engineering Science* 75, pp. 342–348. DOI:
670 10.1016/j.ces.2012.03.011.

671 Herskowitz, M.; Morita, S.; Smith, J. M. (1978): Solubility of hydrogen in.alpha.-methylstyrene. In
672 *Journal of Chemical and Engineering Data* 23 (3).

673 Higbie, R. (1935): The rate of absorption of a pure gas into still liquid during short periods of
674 exposure. In *Transactions of AIChE* 31, 1935.

675 Jejurkar, S. Y.; Khanna, A.; Verma, N. (2020): Maldistribution Effects in an Industrial-Scale Trickle Bed
676 Reactor. In *Ind. Eng. Chem. Res.* 59 (16), pp. 7405–7415. DOI: 10.1021/acs.iecr.0c00115.

677 Lewis, W. K.; Whitman, W. G. (1924): Principles of Gas Absorption. In *Industrial and Engineering*
678 *Chemistry* 16, pp. 1215–1220.

679 Lopes, R. J. G.; Silva, A. M. T.; Quinta-Ferreira, R. M. (2007): Kinetic Modeling and Trickle-Bed CFD
680 Studies in the Catalytic Wet Oxidation of Vanillic Acid. In *Ind. Eng. Chem. Res.* 46 (25), pp. 8380–
681 8387.

682 Lopes, R. J.G.; Quinta-Ferreira, R. M. (2007): Trickle-bed CFD studies in the catalytic wet oxidation of
683 phenolic acids. In *Chemical Engineering Science* 62 (24), pp. 7045–7052. DOI:
684 10.1016/j.ces.2007.08.085.

685 Lopes, Rodrigo J. G.; Quinta-Ferreira, Rosa M. (2010): Assessment of CFD–VOF Method for Trickle-
686 Bed Reactor Modeling in the Catalytic Wet Oxidation of Phenolic Wastewaters. In *Ind. Eng. Chem.*
687 *Res.* 49 (6), pp. 2638–2648. DOI: 10.1021/ie901412x.

688 Marschall, H.; Hinterberger, K.; Schüler, C.; Habla, F.; Hinrichsen, O. (2012): Numerical simulation of
689 species transfer across fluid interfaces in free-surface flows using OpenFOAM. In *Chemical*
690 *Engineering Science* 78, pp. 111–127. DOI: 10.1016/j.ces.2012.02.034.

691 Meier, M.; Yadigaroglu, G.; Smith, B. L. (2002): A novel technique for including surface tension in
692 PLIC-VOF methods. In *European Journal of Mechanics - B/Fluids* 21, pp. 61–73.

693 Meille, V.; de Bellefon, C. (2004): Effect of Water on α -Methylstyrene Hydrogenation on Pd/Al₂O₃. In
694 *The Canadian Journal of Chemical Engineering* 82.

695 Meille, V.; de Bellefon, C.; Schweich, D. (2002): Kinetics of α -Methylstyrene Hydrogenation on
696 Pd/Al₂O₃. In *Ind. Eng. Chem. Res.* 41 (7), pp. 1711–1715. DOI: 10.1021/ie010460g.

697 Nusselt, W. (1916): Die Oberflächenkondensation des Wasserdampfes. In *Zeitschrift des Vereines*
698 *Deutscher Ingenieure*, 1916.

699 Sebastia-Saez, D.; Gu, S.; Ranganathan, P.; Papadikis, K. (2013): 3D modeling of hydrodynamics and
700 physical mass transfer characteristics of liquid film flows in structured packing elements. In
701 *International Journal of Greenhouse Gas Control* 19, pp. 492–502. DOI: 10.1016/j.ijggc.2013.10.013.

702 Sussman, M.; Puckett, E. G. (2000): A Coupled Level Set and Volume-of-Fluid Method for Computing
703 3D and Axisymmetric Incompressible Two-Phase Flows. In *Journal of Computational Physics* 162 (2),
704 pp. 301–337. DOI: 10.1006/jcph.2000.6537.

705 Tourvieille, J. N. (2014): Innovating microstructured gas-liquid-solid reactors: a contribution to the
706 understanding of hydrodynamics and mass transfers.

707 Tourvieille, J. N.; Bornette, F.; Philippe, R.; Vandenberghe, Q.; de Bellefon, C. (2013): Mass transfer
708 characterisation of a microstructured falling film at pilot scale. In *Chemical Engineering Journal* 227,
709 pp. 182–190. DOI: 10.1016/j.cej.2012.07.095.

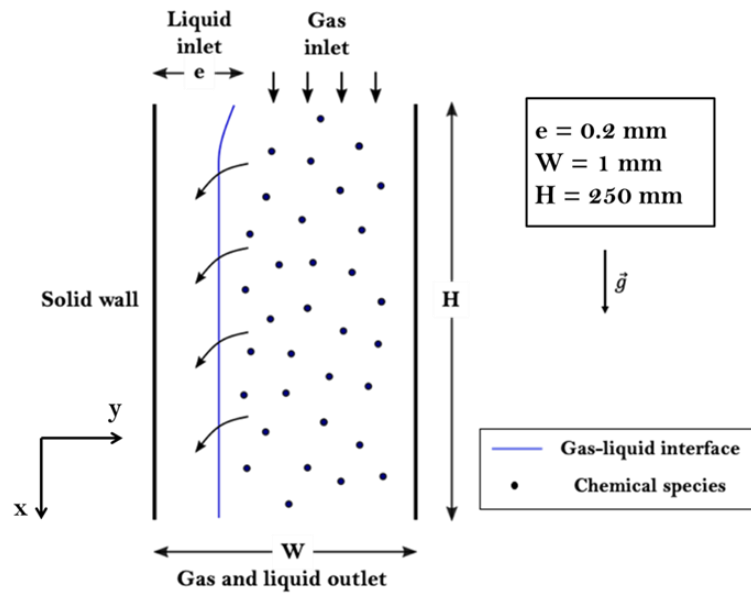
710 Vankayala, B. K.; Löb, P.; Hessel, V.; Menges, G.; Hofmann, C.; Metzke, D. et al.: Scale-up of Process
711 Intensifying Falling Film Microreactors to Pilot Production Scale.

712 Xu, Z. F.; Khoo, B. C.; Wijesundera, N. E. (2008): Mass transfer across the falling film: Simulations
713 and experiments. In *Chemical Engineering Science* 63 (9), pp. 2559–2575. DOI:
714 10.1016/j.ces.2008.02.014.

715 Yeong, K. K.; Gavriilidis, A.; Zapf, R.; Kost, H. J.; Hessel, V.; Boyde, A. (2006): Characterisation of liquid
716 film in a microstructured falling film reactor using laser scanning confocal microscopy. In
717 *Experimental Thermal and Fluid Science* 30 (5), pp. 463–472. DOI:
718 10.1016/j.expthermflusci.2005.09.006.

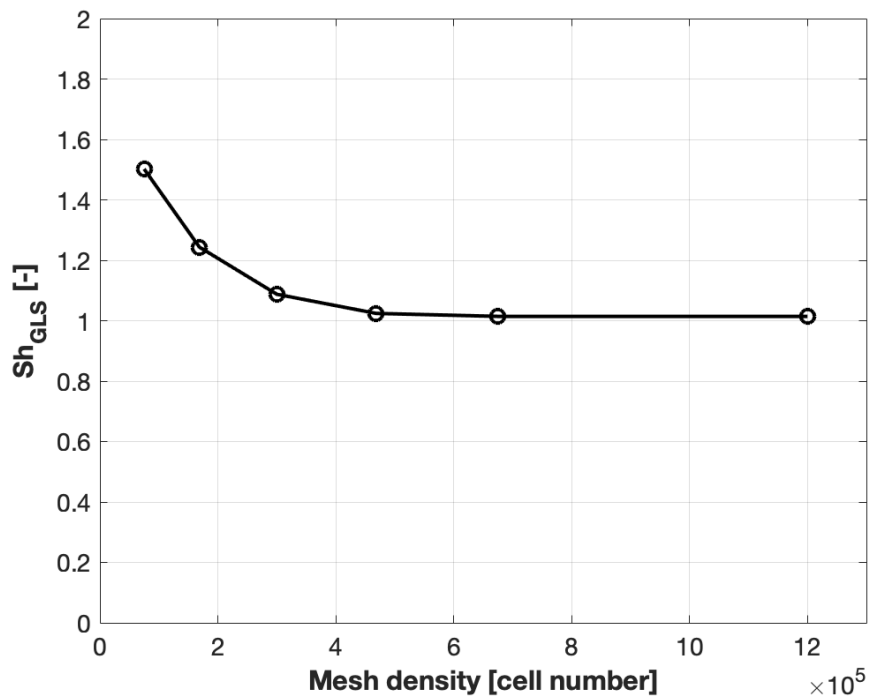
719

720 **Figures**



721

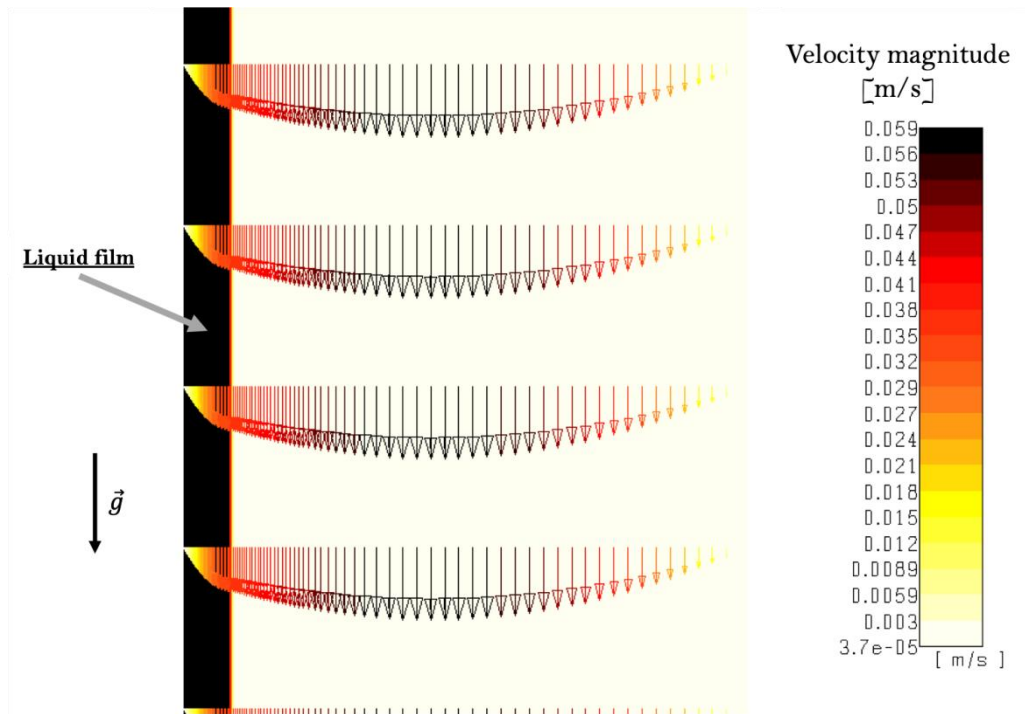
722 **Figure 1: Numerical domain for the 2D liquid falling film over a plane plate**



723

724 **Figure 2 : gas-liquid-solid Sherwood number variation with mesh resolution for a 2D falling liquid film over a vertical**

725 **plane plate**



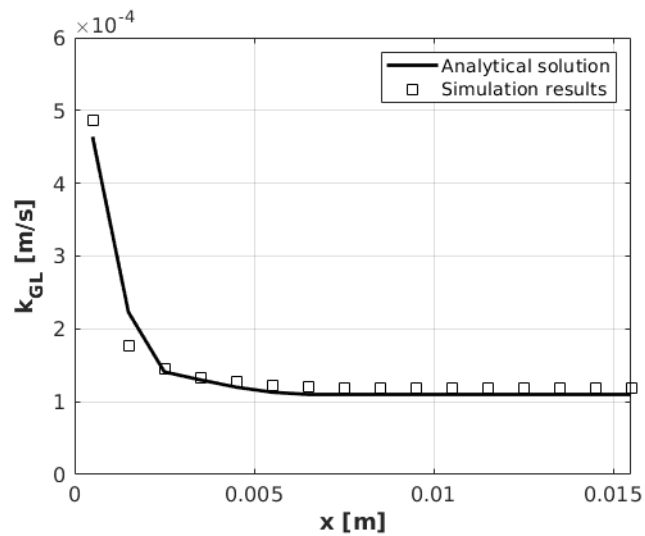
726

727

Figure 3 : Gas volume fraction and velocity vectors for the two-phase flow over a plane plate for $Re_L = 3.98$ and

728

$Re_G = 2.74$ at $T=283K$ and $P=1bar$



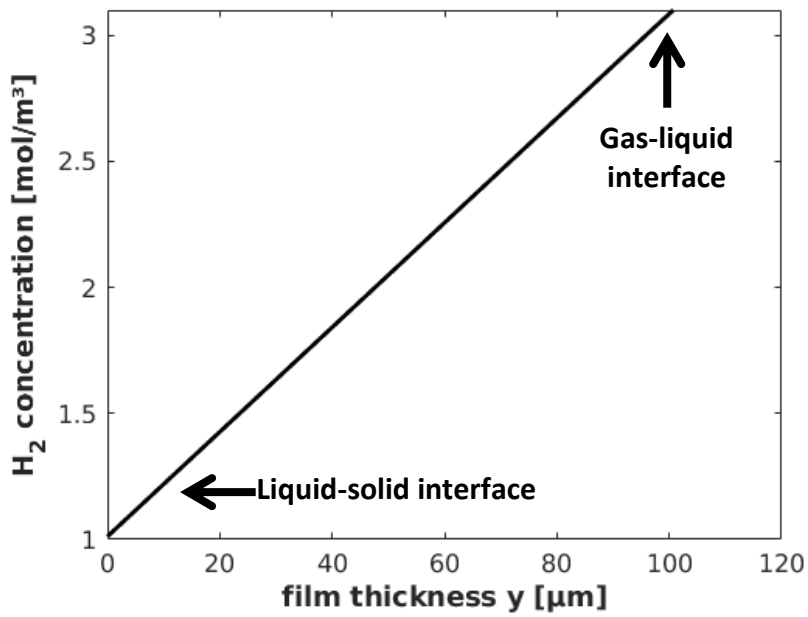
729

730

Figure 4 : analytical and simulated mean gas-liquid mass transfer coefficients for $Re_L = 3.98$ and $Re_G =$

731

2.74 at $T = 283K$ and $P = 1bar$. Analytical values computed using (Higbie 1935)



732

733

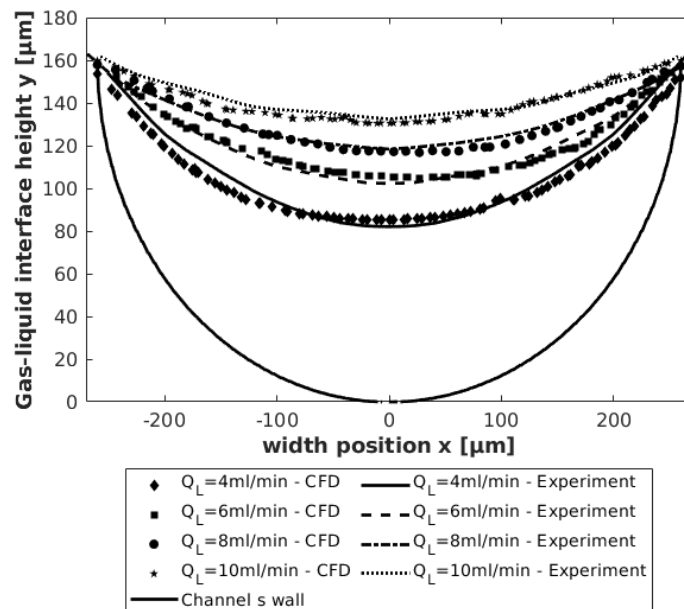
Figure 5 : hydrogen concentration profile in the liquid film in the presence of a heterogeneous catalytic reaction, for

734

$Re_L = 3.98$ and $Re_G = 2.74$ at $T=283K$. The liquid-solid interface is located at $y=0$ and the gas-liquid interface is

735

located at $y=100\mu m$



736

737

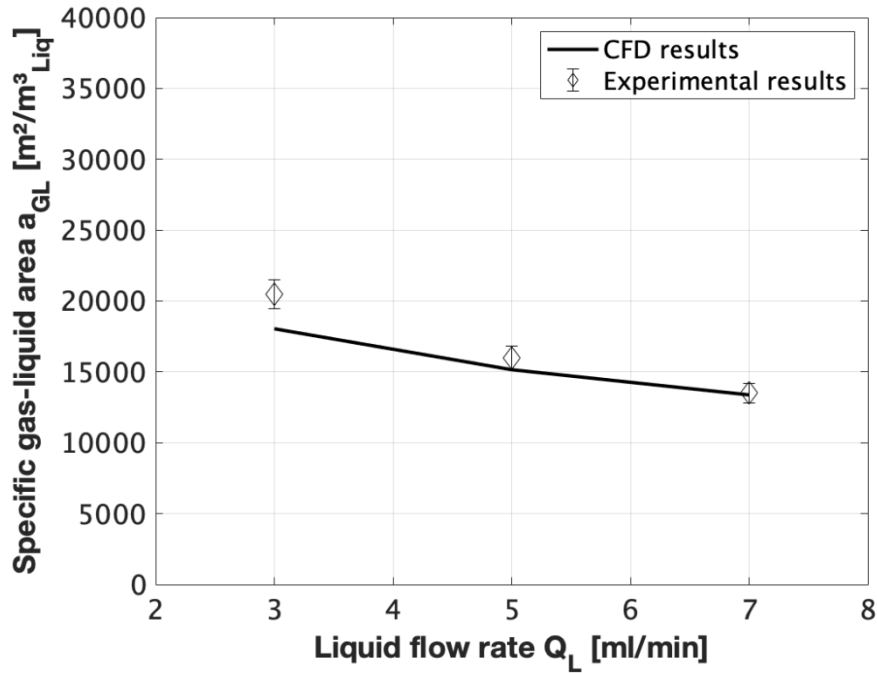
Figure 6 : Comparison between numerical and experimental liquid film profiles for ethanol flow in a $600*200\mu m^2$

738

channel, the liquid flow rate ranges from 4ml/min to 10ml/min. the simulations are performed in isothermal ($T=283K$)

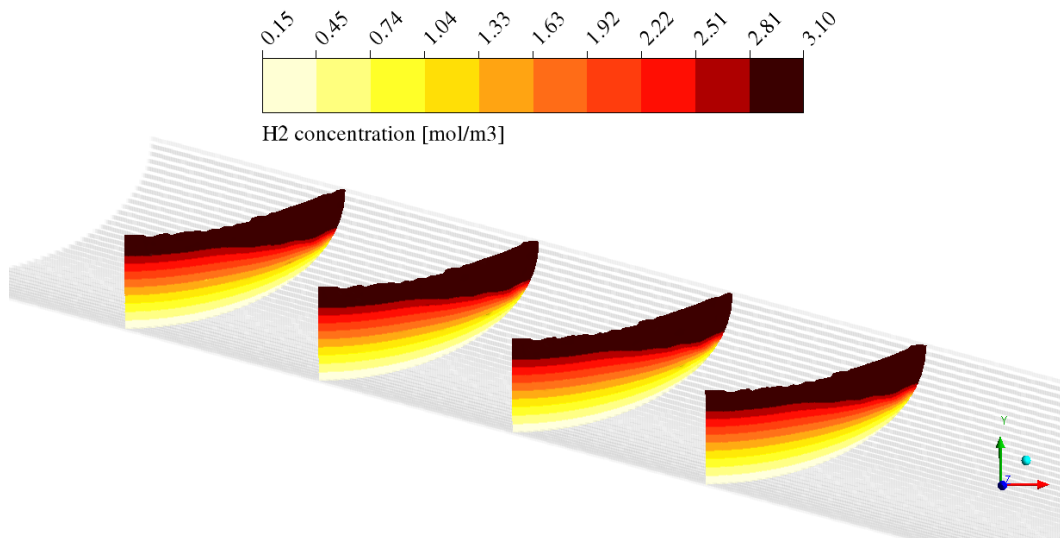
739

and isobaric ($P=1bar$) conditions



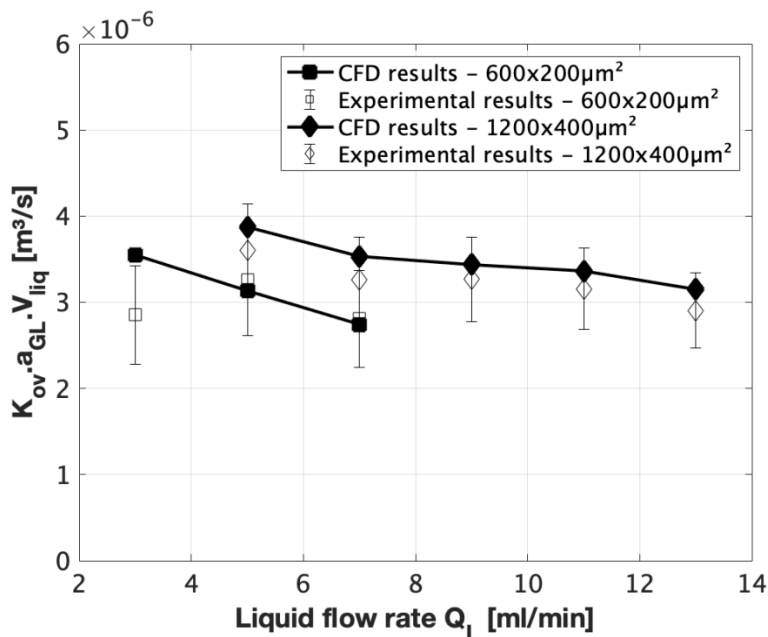
740

741 Figure 7 : Specific gas-liquid area comparison for ethanol/ H_2 flow at Q_L between 3ml/min and 7ml/min in a
 742 $600 \times 200 \mu m^2$ channel, the simulations are performed in isothermal and isobaric conditions ($T=283K$, $P=1bar$). Numerical
 743 results are compared to experimental data of (Tourvieille 2014). Error bars represent $\pm 5\%$

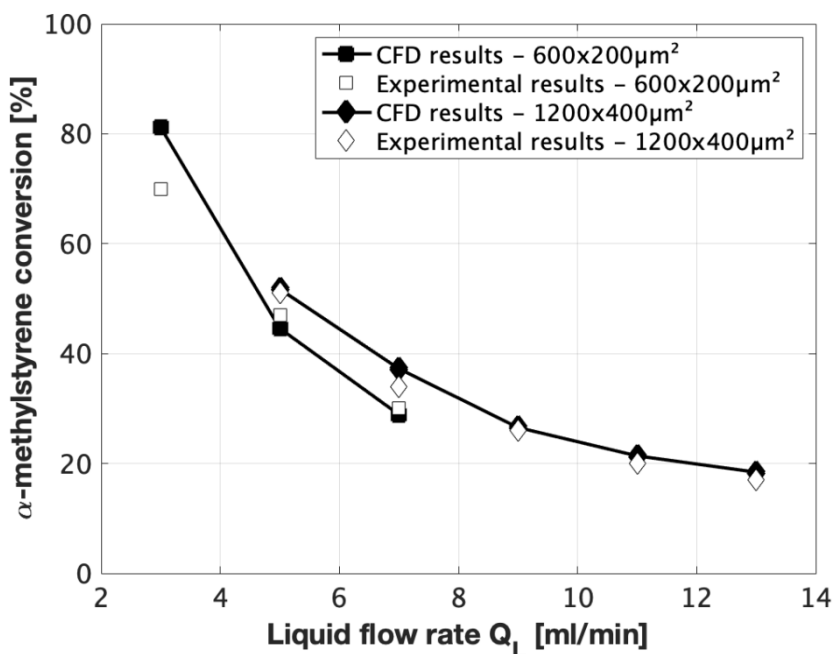


744

745 Figure 8 : concentration profiles in the liquid film for the hydrogenation of α -methylstyrene to cumene in a
 746 $600 \times 200 \mu m^2$ at $Q_L = 7ml/min$, $T=283K$ and $P=5bar$. The outlet plane is located at $z=0mm$, the concentration profiles
 747 are shown from left to right at $z=5mm$, $z=10mm$, $z=15mm$ and $z=20mm$.

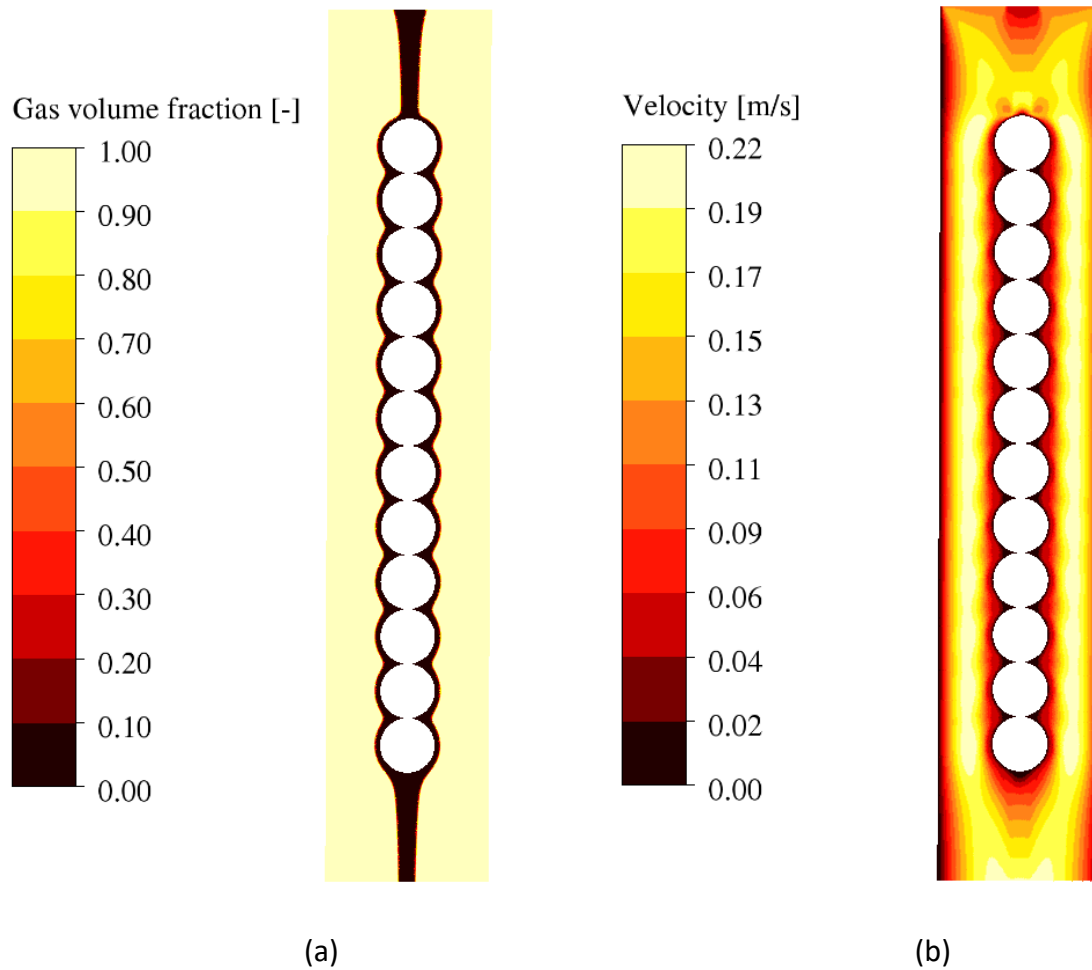


748
749 Figure 9 : Comparison between experimental data and numerical results $K_{ov}a_{GL}V_{liq}$ at $T=283K$ and $P=5bar$. For the
750 $600*200\mu m^2$ channel, the liquid flow rate varies from 3ml/min to 7ml/min and experimental results are drawn from
751 (Tourvieille et al. 2013). For the $1200*400\mu m^2$ channel, the liquid flow rate varies from 5ml/min to 13ml/min and
752 experimental data are drawn from (Tourvieille 2014). Error bars represent $\pm 20\%$



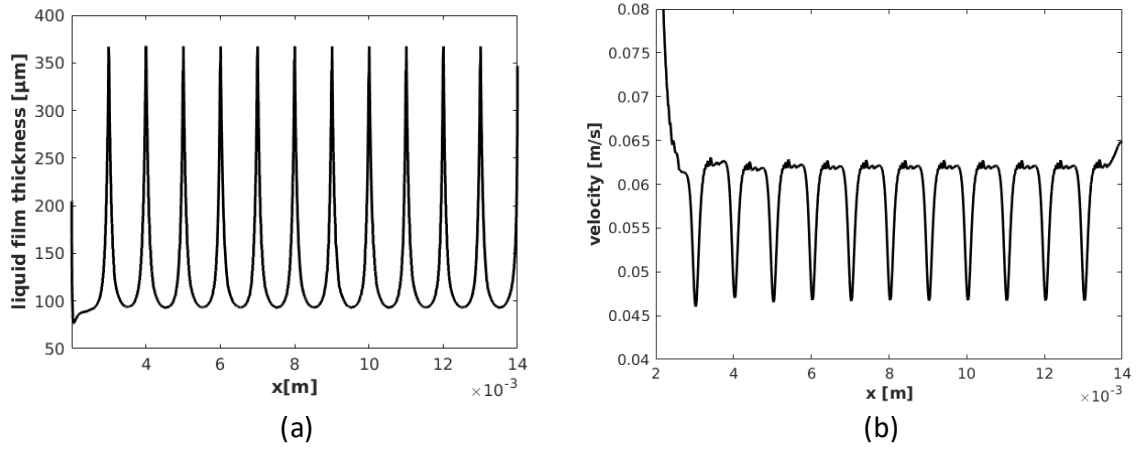
753
754 Figure 10 : α -methylstyrene conversion comparison at $P=5bar$ and $T=283K$, the initial α -methylstyrene is $1mol/m^3$.
755 For the $600*200\mu m^2$ channel, the liquid flow rate varies from 3ml/min to 7ml/min and experimental results are drawn

756 from (Tourvieille et al. 2013). For the $1200 \times 400 \mu\text{m}^2$ channel, the liquid flow rate varies from 5ml/min to 13ml/min and
757 experimental data are drawn from (Tourvieille 2014).



758

759 Figure 11: (a) Liquid volume fraction distribution in $z=0$ plane cut for $Re_G = 25$ and $Re_L = 30$ (b) velocity
760 magnitude profile in $z=0$ plane cut for $Re_G = 25$ and $Re_L = 30$. The two-phase flow is solved in isothermal and isobaric
761 conditions ($T=283\text{K}$ and $P=1\text{bar}$)



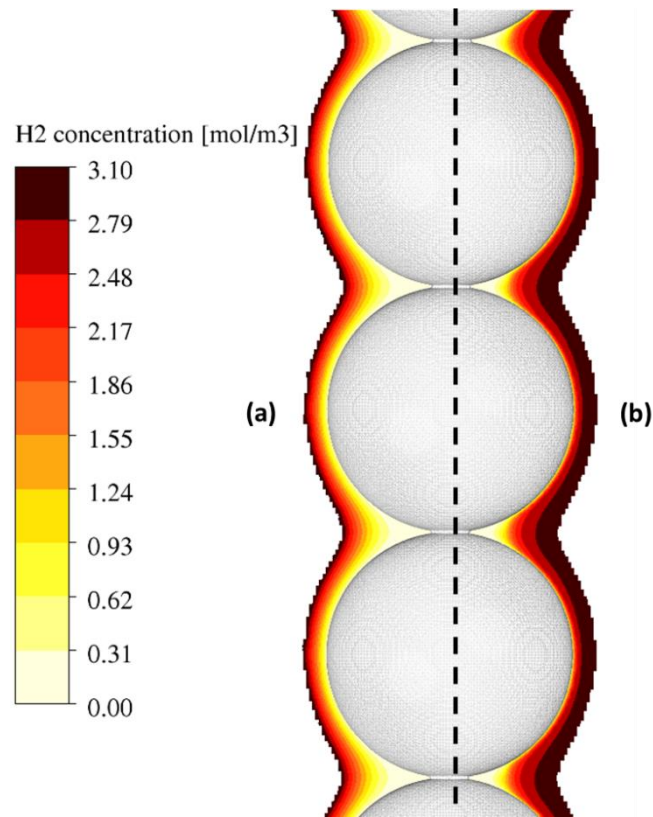
762

763

Figure 12 : (a) liquid film thickness variation and (b) gas-liquid interface velocity variation throughout the domain at

764

$Re_G = 25$ and $Re_L=30$ in isothermal and isobaric conditions ($T=283\text{K}$ and $P=1\text{bar}$)



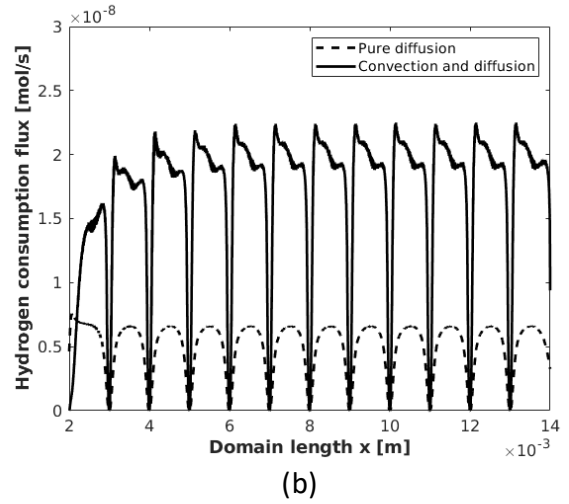
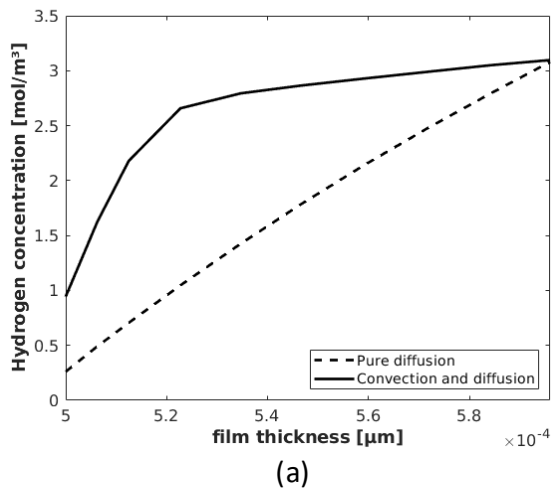
765

766

Figure 13 : Hydrogen concentration profiles at $P=1\text{bar}$, $T=283\text{K}$, $Re_G = 25$ and $Re_L=30$ for (a) pure diffusion (b)

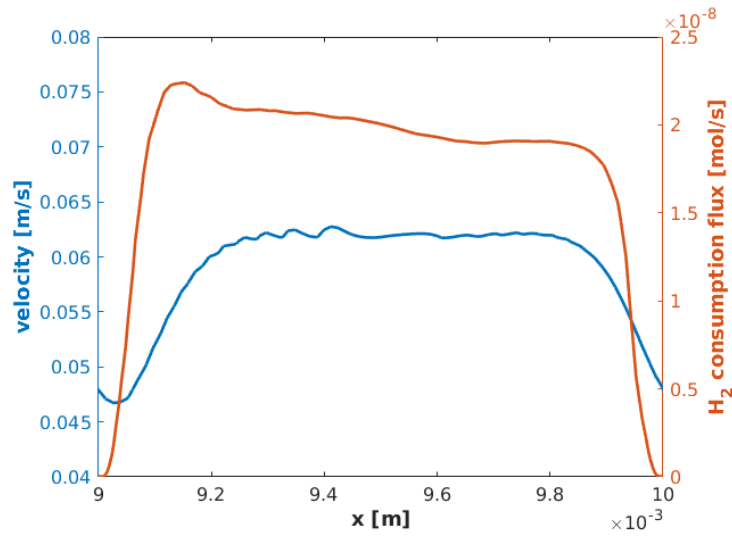
767

convection-diffusion



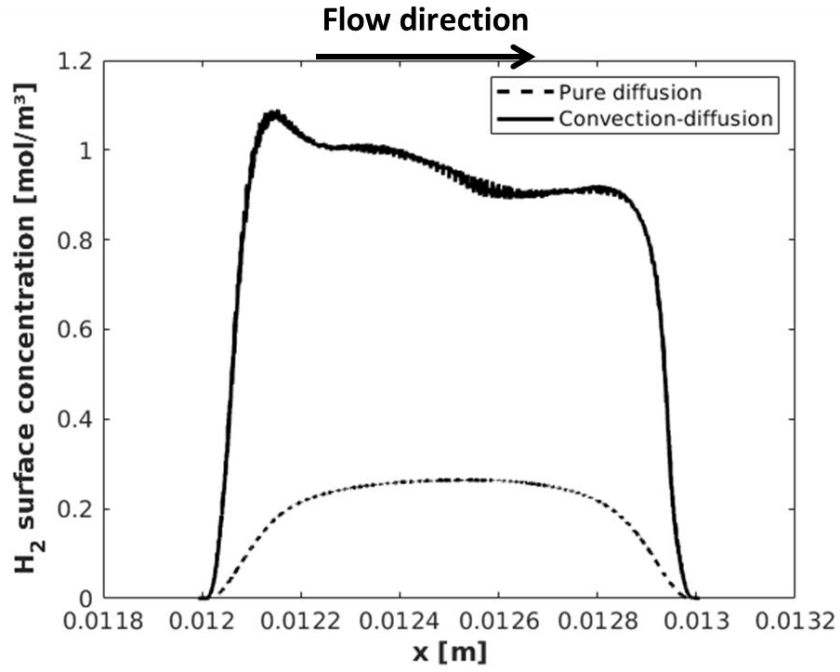
768

769 Figure 14 : (a) Concentration profile comparison at the equatorial plane of the 10th sphere between pure diffusion
 770 conditions and convective-diffusive conditions at $P=1\text{bar}$, $T=283\text{K}$, $Re_G = 25$ and $Re_L=30$ and (b) axial evolution of
 771 hydrogen consumption flux for pure diffusion and convection-diffusion regimes at $P=1\text{bar}$, $T=283\text{K}$, $Re_G = 25$ and
 772 $Re_L=30$



773

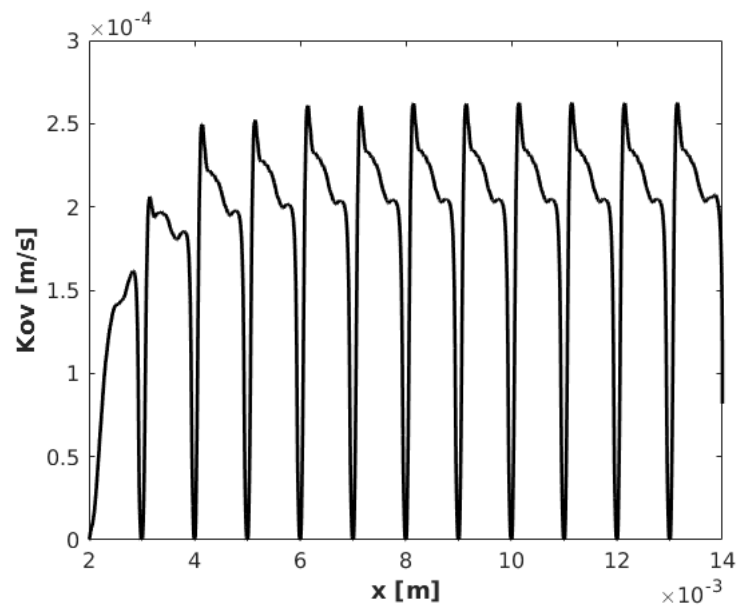
774 Figure 15 : axial evolution of gas-liquid interface velocity magnitude and hydrogen consumption flux variation
 775 throughout one pellet in convection-diffusion regime at $P=1\text{bar}$, $T=283\text{K}$, $Re_G = 25$ and $Re_L=30$



776

777 Figure 16 : Hydrogen surface concentration comparison at the 10th sphere for P=1bar, T=283K, $Re_G = 25$ and

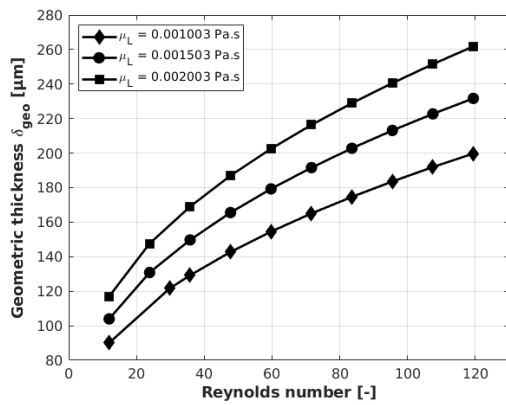
778 $Re_L=30$ for pure diffusion and convection-diffusion conditions



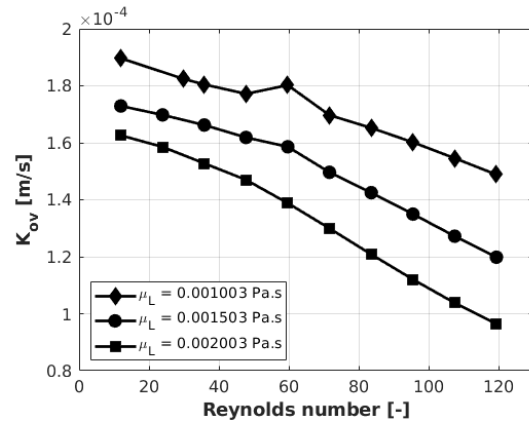
779

780 Figure 17 : overall mass transfer coefficient axial variation throughout the domain in convection-diffusion regime

781 for P=1bar, T=283K, $Re_G = 25$ and $Re_L = 30$



(a)



(b)

782

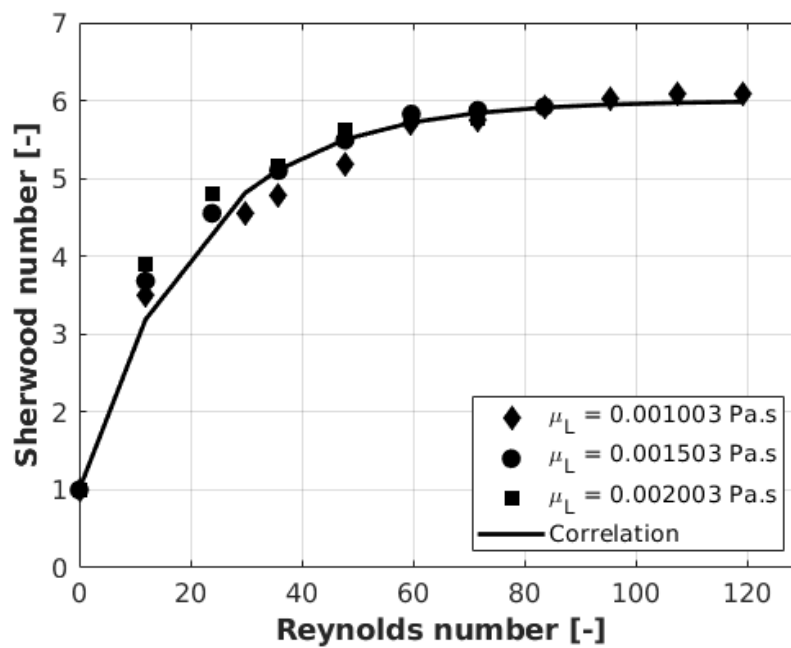
783

Figure 18 : (a) geometric liquid film thickness variation with Reynolds number and liquid viscosity and (b) overall mass transfer coefficient variation with Reynolds number and liquid viscosity in convection-diffusion regime for H₂/methylcyclohexane and α -methylstyrene mixture two-phase flow, for different inlet liquid Reynolds number conditions ($10 < Re_L < 120$) and fixed inlet gas Reynolds number $Re_G = 25$, at P=1bar and T=283K.

784

785

786



787

788

Figure 19 : gas-liquid-solid Sherwood number Sh_{GLS} variation with Reynolds number and liquid viscosity for inlet liquid Reynolds numbers between 0 and 120, inlet gas Reynolds number of $Re_G = 25$, at P=1bar and T=283K.

789

790

791 **Tables**792 **Table 1 : physicochemical properties of the two-phase systems**

	Composition	Operating pressure [bar]	Density ρ [kg/m^3]	Viscosity μ [$kg/m.s$]	Surface tension [N/m]
Gas phase	Pure hydrogen	1	0.086	$8.60 \cdot 10^{-6}$	-
		3	0.26	$8.61 \cdot 10^{-6}$	-
		5	0.43	$8.61 \cdot 10^{-6}$	-
Liquid phase	Water	1, 3 and 5	998	$1.00 \cdot 10^{-3}$	0.072
	Methylcyclohexane and α -methylstyrene (MCH+AMS)		770	$9.10 \cdot 10^{-4}$	0.022
	Ethanol		789	$1.04 \cdot 10^{-3}$	0.0218

793 **Table 2 : Comparison between the numerical and analytical solution for the two-phase flow over a plane plate**

	Analytical solution	Numerical solution	Relative deviation [%]
Interface velocity u_I [cm/s]	3.53	3.54	0.28%
Liquid film thickness β [μm]	85.03	84.62	0.48

794 **Table 3 : film model post-processing data for different pressure conditions**

Pressure (bar)	C^* (mol/m ³)	$K_{ov} \cdot a_{GL}$ (s ⁻¹)	δ_{hydro} (μm)	$\delta_{diffusion}$ (μm)	Relative deviation (%)
1	3.1	0.729	80.4	81.5	1.37%
3	9.4	0.730	80.4	81.5	1.37%
5	16.4	0.729	80.4	81.6	1.50%

795 **Table 4 : Coated plate characteristics used by (Tourvieille et al. 2013) for 600*200 μm^2 channels and (Tourvieille**
796 **2014) for 1200*400 μm^2 channels**

Channel cross section dimensions (μm^2)	600x200	1200x400
channel number per plate	100	50
Catalyst density ρ_{cata} (g/m ³)	690278	737231
Palladium mass fraction W_{Pd} (%)	4.42	4.5
Palladium mass m_{Pd} per plate (mg)	22	49
Catalyst layer volume V_{cata} (cm ³)	0.72	1.46

Catalyst layer thickness (μm)	40	80
--	----	----

797 Table 5 : Summary of experimental and numerical values at P=5bar for the α -methylstyrene hydrogenation to
798 cumene in a $600 \times 200 \mu\text{m}^2$ channel

	Liquid flow rate Q_L (ml/min)	H_2 surface concentration (mol/m ³)	Liquid volume in the reactor (m ³)	H_2 consumption flux (mol/s)	Conversion (%)	$K_{ov} \cdot a_{GL}$ (s ⁻¹)
Experimental values	3	4.30	$5.60 \cdot 10^{-7}$	$3.46 \cdot 10^{-5}$	70%	5.10
	5	4.80	$6.80 \cdot 10^{-7}$	$3.79 \cdot 10^{-5}$	47%	4.80
	7	4.30	$7.80 \cdot 10^{-7}$	$3.40 \cdot 10^{-5}$	30%	3.60
Numerical values	3	4.97	$8.24 \cdot 10^{-7}$	$4.06 \cdot 10^{-5}$	81%	4.31
	5	4.55	$9.70 \cdot 10^{-7}$	$3.71 \cdot 10^{-5}$	45%	3.23
	7	4.11	$1.08 \cdot 10^{-6}$	$3.37 \cdot 10^{-5}$	29%	2.54

799 Table 6 : comparison of GLS mass transfer coefficients $K_{ov} \cdot a_{GL}$ to the ones obtained by the resistances-in-series
800 model $K_R \cdot a_{GL}$ in isothermal conditions (T=283K), for pressure conditions from 1bar to 5bar, and liquid flow rate
801 conditions from 3ml/min to 7ml/min.

Pressure (bar)	C^* (mol/m ³)	Liquid flow (mL/min)	$K_{ov} \cdot a_{GL}$ (s ⁻¹)	$K_R \cdot a_{GL}$ (s ⁻¹)	Relative error (%)
1	3.1	3ml/min	1.78	1.19	33%
		5ml/min	1.23	0.86	31%
		7ml/min	0.98	0.77	21%
3	9.4	3ml/min	1.77	1.19	33%
		5ml/min	1.22	0.85	30%
		7ml/min	0.97	0.74	24%
5	16.4	3ml/min	1.75	1.19	32%
		5ml/min	1.21	0.85	29%
		7ml/min	0.96	0.74	24%

802 Table 7 : Film model optimization data in a $600 \times 200 \mu\text{m}^2$ channel for liquid flow rates between 3ml/min and
803 7ml/min, pressure conditions between 1bar and 5bar, at fixed operating temperature (T=283K)

		δ_C	δ_A	δ_{geo}	δ_H
Film model $K_{ov,FM} = D/\delta$	Mean relative deviation [%]	32.99%	10.64%	30.24%	113.71%
Modified film model $K'_{ov,FM} = A \cdot D/\delta$	Correction factor A [-]	1.479	1.112	1.405	0.469
	Mean relative deviation [%]	1.85%	1.48%	3.72%	6.66%

804 Table 8: comparison of GLS mass transfer coefficients $K_{ov} \cdot a_{GL}$ to the ones obtained by the resistances-in-series
 805 model $K_R a_{GL}$ in isothermal conditions (T=283K), for pressure conditions from 1bar to 5bar, at $Re_G = 25$ and $Re_L = 30$.

Pressure (bar)	C^* (mol/m ³)	$K_{ov} \cdot a_{GL}$ (s ⁻¹)	$K_R \cdot a_{GL}$ (s ⁻¹)	Relative error (%)
1	3.1	2.60	1.90	36%
3	9.4	2.60	1.89	37%
5	16.4	2.60	1.89	37%

806 Table 9 : overall external mass transfer post-processing data in convection-diffusion and pure diffusion regimes at
 807 $1 < P(\text{bar}) < 5$, T=283K, $Re_G = 25$ and $Re_L = 30$.

Convection and diffusion					
Pressure (bar)	C_S (mol/m ³)	Reaction flux (mol/s)	K_{ov} (m. s ⁻¹)	δ_{app} [μm]	δ_{geo} [μm]
1	0.84	$1.47 \cdot 10^{-9}$	$1.83 \cdot 10^{-4}$	26.59	122.72
3	2.84	$4.22 \cdot 10^{-9}$	$1.82 \cdot 10^{-4}$	26.78	122.72
5	5.23	$7.16 \cdot 10^{-9}$	$1.82 \cdot 10^{-4}$	26.87	122.72
Pure diffusion					
Pressure (bar)	C_S CFD (mol/m ³)	Reaction flux (mol/s)	K_{ov} (m. s ⁻¹)	δ_{app} [μm]	δ_{geo} [μm]
1	0.19	$4.11 \cdot 10^{-10}$	$4.01 \cdot 10^{-5}$	121.63	122.72
3	0.69	$1.23 \cdot 10^{-9}$	$4.01 \cdot 10^{-5}$	121.92	122.72
5	1.30	$2.13 \cdot 10^{-9}$	$3.99 \cdot 10^{-5}$	122.08	122.72

808